Supporting Material

A Set of Basic Homeostatic Controller Motifs

T. Drengstig[1], I. W. Jolma[2], X. Y. Ni[2],
K. Thorsen[1], X. M. Xu[2], and P. Ruoff[2,*]

[1]Department of Electrical Engineering and Computer Science,
[2]Centre for Organelle Research
University of Stavanger, Stavanger, Norway

[*]Corresponding author. Address: Centre for Organelle Research, University of Stavanger, N-4036 Stavanger, Norway, Tel.: (47) 5183-1887, Fax: (47) 5183-1750, E-mail: peter.ruoff@uis.no

Constructing the Set of Controller Motifs

We consider two molecular components, A and E, which mutually affect each other's synthesis or degradation by either activating them (indicated by a dashed arrow with a positive sign) or by inhibiting them (indicated by a dashed negative inhibition sign).

The type of feedback (i.e., positive or negative) for a particular motif can be determined as illustrated in Fig. S1 (this example is motif 5 in Fig. S2).

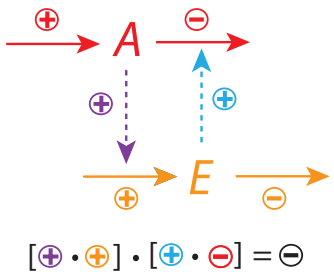

Figure S1: Illustrating how to determine the type of feedback.

Starting from component A and moving along the loop while multiplying the plus/minus signs of the activation/inhibition steps with the positive/negative signs of the synthesis/degradation reaction of the other component leads to the sign of the feedback loop, which in case of the motif in Fig. S1 is negative.

The controller motifs are constructed in the following way: from E and A, inhibition or activation signals act on the other species' synthesis or degradation processes, but not on both. Because A can affect E by four different combinations (i.e., by activating or inhibiting E's synthesis or degradation) and E can affect A likewise, we get in total 16 different motifs. Eight of these motifs on which we focus here are negative feedback loops (Fig. S2), while the remaining eight are positive feedbacks (Fig. S3).

Computational Methods

The rate equations were solved by using Matlab/Simulink (www.mathworks.com) and the Fortran subroutine LSODE (1). To ensure that correct steady state values are obtained the simulation times were varied and results inspected.

The perturbations in A, i.e. the uncontrolled addition or removal of A in the various controller motifs have been formulated as zero-order and first-order kinetics with rate constants k_{pert}^{inflow} and $k_{pert}^{outflow}$, respectively

$$\dot{A} = k_{pert}^{inflow} - k_{pert}^{outflow} \cdot A + j_A \tag{S1}$$

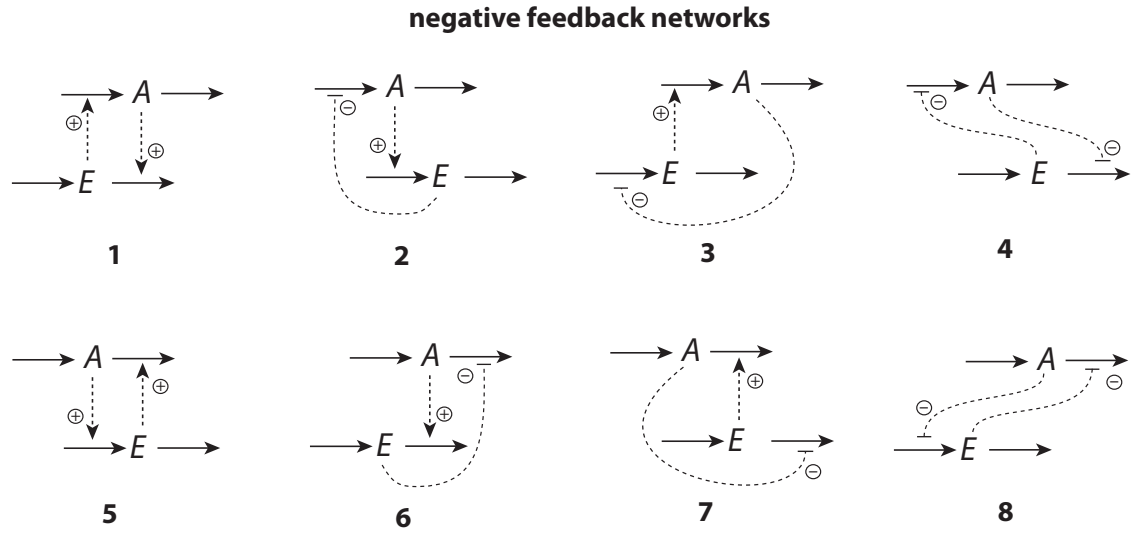

Figure S2: Network motifs with negative feedback.

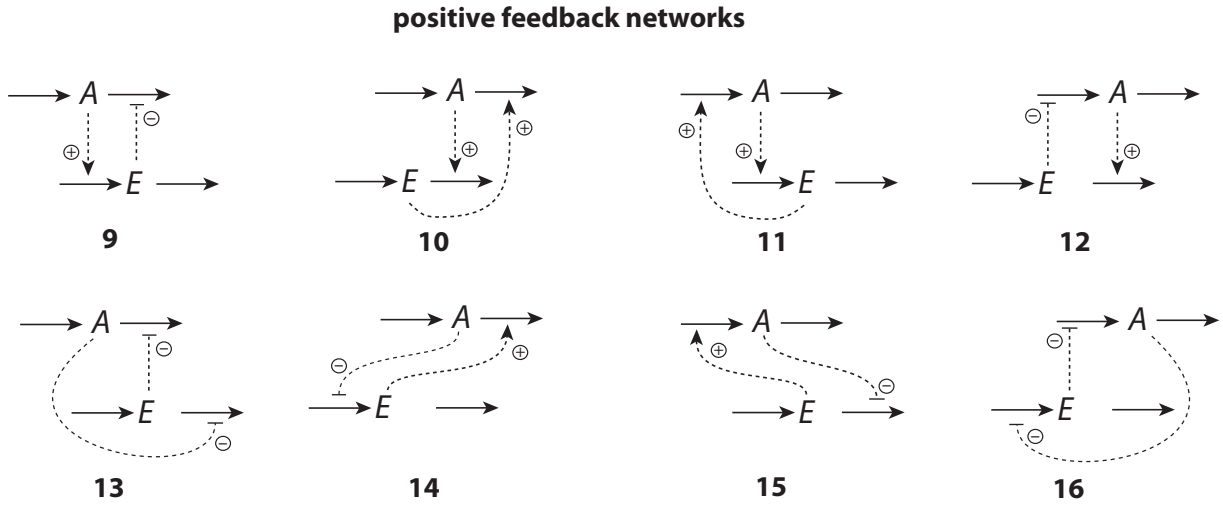

Figure S3: Network motifs with positive feedback.

or

$$\dot{A} = k_{pert}^{inflow} - k_{pert}^{outflow} \cdot A - j_A \tag{S2}$$

where j_A denote the E-mediated compensatory fluxes for inflow controllers (Eq. S1) or for outflow controllers (Eq. S2).

The compensatory fluxes in A from an external A-source (A_{ext}) or out of the system are described by Michaelis-Menten kinetics with respect to A_{ext} for inflow controllers and with respect to internal A for outflow controllers. For the sake of simplicity external A-levels, A_{ext}, are kept constant. The kinetics of j_A with respect to E can take different forms; E-activated j_A fluxes have (for the sake of simplicity) been formulated mostly as first-order kinetics with respect to E, although an expression with saturation kinetics, $j_A = j_{A,max} \cdot E/(K_a^E + E)$ has also been explored (see *Performance of individual controllers* in main paper). The E-inhibiting fluxes j_A are described by the expression $j_A = j_{A,max} \cdot K_I^E/(K_I^E + E)$. Examples of how E-activating and E-inhibiting j_A fluxes can be obtained are given in the next two sections.

Kinetics of E-activating j_A flux

We consider a mechanism where E activates a transporter T, which then transports external A, A_{ext}, into the cell

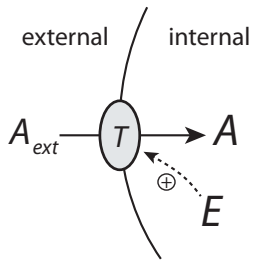

Figure S4: Schematic drawing showing transporter T activated by E and transporting external A (A_{ext}) into the cell.

In the mechanism T binds first A_{ext}, described as the following rapid equilibrium

$$A_{ext} + T \rightleftharpoons A_{ext} \cdot T$$

with the dissociation constant $K_d^{A_{ext} \cdot T}$ given as:

$$K_d^{A_{ext} \cdot T} = \frac{(A_{ext}) \cdot (T)}{(A_{ext} \cdot T)} \tag{S3}$$

The complex $A_{ext} \cdot T$ binds then E, leading to the ternary complex $A_{ext} \cdot T \cdot E$,

$$A_{ext}{\cdot}T + E \rightleftharpoons A_{ext}{\cdot}T{\cdot}E$$

For the sake of simplicity a rapid equilibrium is also assumed for this step with the following dissociation (Michaelis) constant K_M:

$$K_M = \frac{(A_{ext}{\cdot}T){\cdot}(E)}{(A_{ext}{\cdot}T{\cdot}E)} \tag{S4}$$

The transport of A occurs by the following reaction step (with rate constant k_{cat}), with the release of T and E

$$A_{ext}{\cdot}T{\cdot}E \rightarrow A + T + E$$

The compensatory flux j_A can then be written as

$$j_A = k_{cat} \cdot (A_{ext}{\cdot}T{\cdot}E) \tag{S5}$$

To get an expression of how j_A depends on the concentration of E, and A_{ext}, the total concentration of transporter T, $(T)_0$, is calculated, i.e.,

$$(T)_0 = (T) + (A_{ext}{\cdot}T) + (A_{ext}{\cdot}T{\cdot}E) \tag{S6}$$

By use of Eqs. S3 and S4, $(T)_0$ can be written as

$$\begin{aligned}(T)_0 &= \frac{K_d^{A_{ext}{\cdot}T}}{(A_{ext})} \cdot (A_{ext}{\cdot}T) + (A_{ext}{\cdot}T) + (A_{ext}{\cdot}T{\cdot}E) \\ &= \frac{K_d^{A_{ext}{\cdot}T}}{(A_{ext})} \cdot \frac{K_M}{(E)} \cdot (A_{ext}{\cdot}T{\cdot}E) + \frac{K_M}{(E)} \cdot (A_{ext}{\cdot}T{\cdot}E) + (A_{ext}{\cdot}T{\cdot}E)\end{aligned} \tag{S7}$$

Solving Eq. S7 for the concentration of the ternary complex $A_{ext}{\cdot}T{\cdot}E$, and multiplying it with k_{cat} gives the expression for j_A

$$\begin{aligned}j_A &= \frac{k_{cat}{\cdot}(T)_0}{1 + \frac{K_M}{(E)}\left(1 + \frac{K_d^{A_{ext}{\cdot}T}}{(A_{ext})}\right)} \\ &= j_{A,max} \cdot \frac{(E)}{K_a^E + (E)}\end{aligned} \tag{S8}$$

where $j_{A,max} = k_{cat}{\cdot}(T)_0$ and $K_a^E = K_M\left(1 + \frac{K_d^{A_{ext}{\cdot}T}}{(A_{ext})}\right)$.

Kinetics of E-inhibiting j_A flux

In this mechanism, external A binds to transporter T, which then transfers A into the interior of the cell, but E inhibits this process.

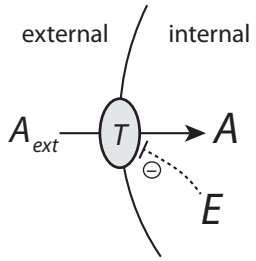

Figure S5: Transporter T transports A_{ext} into the cell and is inhibited by E.

The binding of A_{ext} is described again by the rapid equilibrium

$$A_{ext} + T \rightleftharpoons A_{ext}{\cdot}T$$

with the dissociation constant $K_d^{A_{ext}\cdot T}$ given in Eq. S3. The compensatory flux j_A is given by the expression

$$j_A = k_{cat} \cdot (A_{ext}{\cdot}T) \tag{S9}$$

The inhibition by E is due its binding to $A_{ext}{\cdot}T$ leading to the inactive ternary complex $A_{ext}{\cdot}T{\cdot}E$. The binding is described by a rapid equilibrium with dissociation constant K_I^E

$$K_I^E = \frac{(A_{ext}{\cdot}T){\cdot}(E)}{(A_{ext}{\cdot}T{\cdot}E)} \tag{S10}$$

Using Eq. S6, the total concentration of transporter T can be expressed as a function of the concentration of $A_{ext}{\cdot}T$

$$(T)_0 = \frac{K_d^{A_{ext}\cdot T}}{(A_{ext})} \cdot (A_{ext}{\cdot}T) + (A_{ext}{\cdot}T) + \frac{(E)}{K_I^E}(A_{ext}{\cdot}T) \tag{S11}$$

Solving for $A_{ext}{\cdot}T$ and inserting it into Eq. S9 gives

$$j_A = \frac{k_{cat} \cdot (T)_0}{\left(1 + \frac{K_d^{A_{ext}\cdot T}}{(A_{ext})}\right) + \frac{(E)}{K_I^E}}$$

When the binding between external A and T is strong, i.e., $K_d^{A_{ext}\cdot T} \to 0$, then

$$j_A = j_{A,max} \cdot \frac{K_I^E}{K_I^E + E} \tag{S12}$$

where $j_{A,max} = k_{cat} \cdot (T)_0$.

Steady State Behaviors of Single Controller Motifs

In the following the rate equations and the homeostatic behaviors for each controller motif is given, where function $f(E)$ is defined as $f(E)=\frac{E}{K_M^{E_{set}}+E}$.

Inflow Controller Motifs

Controller Motif 1

The motif and rate equations are:

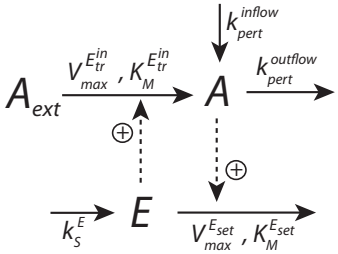

$$\dot{A} = \frac{V_{max}^{E_{tr}^{in}} \cdot A_{ext}}{(K_M^{E_{tr}^{in}} + A_{ext})} \cdot E + k_{pert}^{inflow} - k_{pert}^{outflow} \cdot A \tag{S13}$$

$$\dot{E} = k_s^E - \frac{V_{max}^{E_{set}} \cdot E}{K_M^{E_{set}} + E} \cdot A \tag{S14}$$

Following the outline in the main paper, the theoretic set-point of this controller is given by

$$A_{set} = \frac{k_s^E}{V_{max}^{E_{set}}} \tag{S15}$$

leading to the following integral feedback control structure:

$$\dot{E} = V_{max}^{E_{set}} \left(\frac{k_s^E}{V_{max}^{E_{set}}} - f(E) \cdot A \right) \tag{S16}$$

where $K_i = V_{max}^{E_{set}}$ and $A_{meas} = f(E) \cdot A$ as shown in Table 1 in main paper.

Controller Motif 2

The rate equations for motif 2 are:

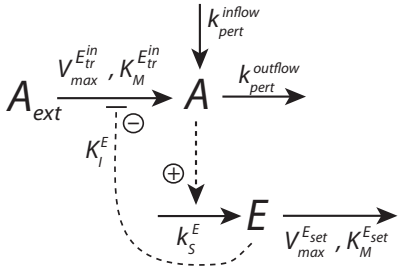

$$\dot{A} = \frac{V_{max}^{E_{tr}^{in}} \cdot A_{ext}}{(K_M^{E_{tr}^{in}} + A_{ext})} \cdot \frac{K_I^E}{(K_I^E + E)} + k_{pert}^{inflow} - k_{pert}^{outflow} \cdot A \tag{S17}$$

$$\dot{E} = k_s^E \cdot A - \frac{V_{max}^{E_{set}} \cdot E}{K_M^{E_{set}} + E} \tag{S18}$$

The theoretic set-point of this controller motif is given by

$$A_{set}=\frac{V_{max}^{E_{set}}}{k_s^E} \tag{S19}$$

leading to the following integral feedback control structure:

$$\dot{E} = -k_s^E \cdot f(E) \left(\frac{V_{max}^{E_{set}}}{k_s^E} - \frac{A}{f(E)} \right) \tag{S20}$$

where $K_i = -k_s^E \cdot f(E)$ and $A_{meas}=\frac{A}{f(E)}$ as shown in Table 1 in main paper.

Controller Motif 3

The rate equations for motif 3 are:

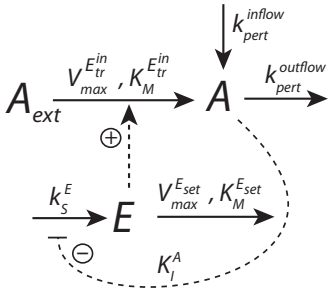

$$\dot{A} = \frac{V_{max}^{E_{tr}^{in}} \cdot A_{ext}}{(K_M^{E_{tr}^{in}} + A_{ext})} \cdot E + k_{pert}^{inflow} - k_{pert}^{outflow} \cdot A \tag{S21}$$

$$\dot{E} = k_s^E \cdot \frac{K_I^A}{K_I^A + A} - \frac{V_{max}^{E_{set}} \cdot E}{K_M^{E_{set}} + E} \tag{S22}$$

The theoretic set-point of this controller motif is given by

$$A_{set} = \frac{k_s^E \cdot K_I^A}{V_{max}^{E_{set}}} - K_I^A \tag{S23}$$

To cast $\dot{E}$ in form of a standard integral control law, we first write:

$$\dot{E} = \frac{V_{max}^{E_{set}}}{K_I^A + A} \left(\frac{k_s^E \cdot K_I^A}{V_{max}^{E_{set}}} - (K_I^A + A) \cdot f(E) \right)$$

Finally, we add and subtract $K_I^A \cdot (1 - f(E))$ inside the parentheses and get:

$$\dot{E} = \frac{V_{max}^{E_{set}}}{K_I^A + A} \cdot \left(\frac{k_s^E \cdot K_I^A}{V_{max}^{E_{set}}} - K_I^A - \Big(f(E) \cdot (K_I^A + A) - K_I^A \Big) \right) \tag{S24}$$

where $K_i = \frac{V_{max}^{E_{set}}}{K_I^A + A}$ and $A_{meas} = f(E) \cdot (K_I^A + A) - K_I^A$, as shown in Table 1 in main paper.

Controller Motif 4

The rate equations for motif 4 are:

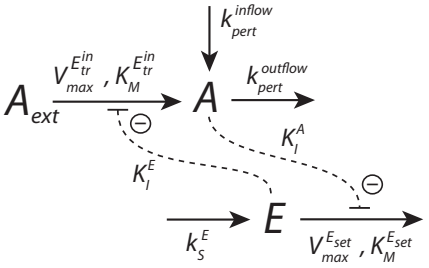

$$\dot{A} = \frac{V_{max}^{E_{tr}^{in}} \cdot A_{ext}}{(K_M^{E_{tr}^{in}} + A_{ext})} \cdot \frac{K_I^E}{(K_I^E + E)} + k_{pert}^{inflow} - k_{pert}^{outflow} \cdot A \tag{S25}$$

$$\dot{E} = k_s^E - \frac{V_{max}^{E_{set}} \cdot E}{(K_M^{E_{set}} + E)} \cdot \frac{K_I^A}{(K_I^A + A)} \tag{S26}$$

The theoretic set-point of this controller motif is given by

$$A_{set} = \frac{V_{max}^{E_{set}} \cdot K_I^A}{k_s^E} - K_I^A \tag{S27}$$

To cast $\dot{E}$ in form of a standard integral control law, we write:

$$\dot{E} = -\frac{k_s^E}{K_I^A + A} \cdot f(E) \cdot \left(\frac{V_{max}^{E_{set}} \cdot K_I^A}{k_s^E} - \frac{(K_I^A + A)}{f(E)} \right)$$

Adding and subtracting K_I^A inside the parentheses leads finally to:

$$\dot{E} = -\frac{k_s^E}{K_I^A + A} \cdot f(E) \cdot \left(\frac{V_{max}^{E_{set}} \cdot K_I^A}{k_s^E} - K_I^A - \left(\frac{(K_I^A + A)}{f(E)} - K_I^A \right) \right) \tag{S28}$$

where $K_i = -\frac{k_s^E}{K_I^A + A} \cdot f(E)$ and $A_{meas} = \frac{(K_I^A + A)}{f(E)} - K_I^A$, as shown in Table 1 in main paper.

Steady state values of activating and inhibiting inflow controllers

Reference is made to Fig. 2 in the main paper. The parameter values for the inflow 1 controller (adding subscript 1 to the parameters and variables in Eqs. S13 and S14 for unique identification) are $k_s^{E_1}$=1.0, $V_{max}^{E_{set,1}}$=0.5, $K_M^{E_{set,1}}$=1·10^{-3}, $V_{max}^{E_{tr}^{in,1}}$=0.5 and $K_M^{E_{tr}^{in,1}}$=1·10^{-4}.

The parameter values for the inflow 2 controller (adding subscript 2 to the parameters and variables in Eqs. S17 and S18 for unique identification) are $k_s^{E_2}$=0.5, $V_{max}^{E_{set,2}}$=1.0, $K_M^{E_{set,2}}$=1·10^{-3}, $V_{max}^{E_{tr}^{in,2}}$=10.0, $K_M^{E_{tr}^{in,2}}$=1·10^{-4} and $K_I^{E_2}$=1·10^{-2}. Initial concentrations: A_{ext}=2.0, A=0.0, E_1=1.0, and E_2=1.0. The perturbations k_{pert}^{inflow} and $k_{pert}^{outflow}$ are varied between 1 and 7 with interval of 0.2.

Fig. 2a in the main paper (reprinted in Fig. S6) shows the steady state values in A when using an E-activating inflow controller (motif 1) compared to an E-inhibiting inflow controller (motif 2).

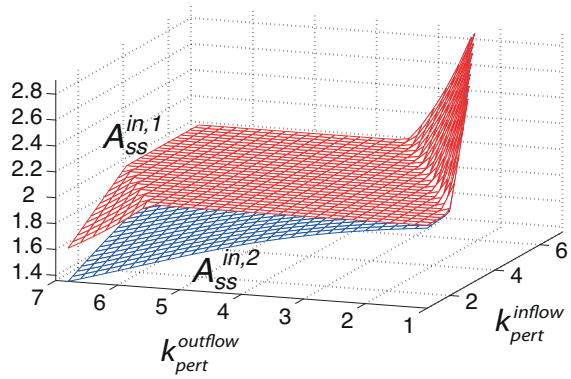

Figure S6: Steady state levels of A ($A_{ss}^{in,1}$ and $A_{ss}^{in,2}$) using inflow controller motif 1 and 2, respectively. The homeostatic set-points are $A_{set}^{in,1} = A_{set}^{in,2} = 2.0$. The better homeostatic performance of motif 1 compared to motif 2 is clearly seen. This is due to first order kinetics in j_A with respect to E_1 . The loss of homeostasis for motif 1 at high $k_{pert}^{outflow}$ values (seen as a bend in $A_{ss}^{in,1}$) is due to the introduction of an upper bound in E_1 (see Fig. 2, main paper).

However, the first-order kinetics with respect to E_1 in the compensatory flux j_A of inflow controller motif 1 (Eq. S13) represents an idealization, because j_A does not go into saturation (as the compensatory flux of inflow controller motif 2 does, see Eq. S17), unless an upper bound in $E_!$ is introduced for controller 1 as shown in Fig. 2 in the main paper.

As signal transduction processes are mediated by binding events between molecules, a more realistic representation of the E-activating compensatory fluxes is given by Eq. S8 where

$$j_{A,max} = \frac{V_{max}^{E_{tr}^{in}} \cdot A_{ext}}{(K_M^{E_{tr}^{in}} + A_{ext})} \tag{S29}$$

In the following we compare controllers 1 and 2 when using $j_A = j_{A,max} \cdot E_1/(K_a^{E_1} + E_1)$ and $j_A = j_{A,max} \cdot K_I^{E_2}/(K_I^{E_2} + E_2)$, respectively. In these calculations the rate equation of A for controller 1, Eq. S13, is now replaced by:

$$\dot{A} = j_{A,max} \cdot \frac{E_1}{K_a^{E_1} + E_1} + k_{pert}^{inflow} - k_{pert}^{outflow} \cdot A \tag{S30}$$

For the sake of simplicity A_{ext} in Eq. S29 is considered as a constant, which leads to a constant $j_{A,max}$. The rate equations for controller motif 2 are as described by Eqs. S17 and S18.

The parameter values for inflow 1 controller are: $k_s^{E_1}$=1.0, $V_{max}^{E_{set,1}}$=0.5, $K_M^{E_{set,1}}$=1·10^{-3}, $V_{max}^{E_{tr}^{in,1}}$ =10, $K_M^{E_{tr}^{in,1}}$ =1·10^{-4}, and K_a^E = 0.1. The parameter values for the inflow 2 controller are: $k_s^{E_2}$=0.5, $V_{max}^{E_{set,2}}$=1.0, $K_M^{E_{set,2}}$=1·10^{-3}, $V_{max}^{E_{tr}^{in,2}}$ =10.0, $K_M^{E_{tr}^{in,2}}$ =1·10^{-4}, and $K_I^{E_2}$=0.1.

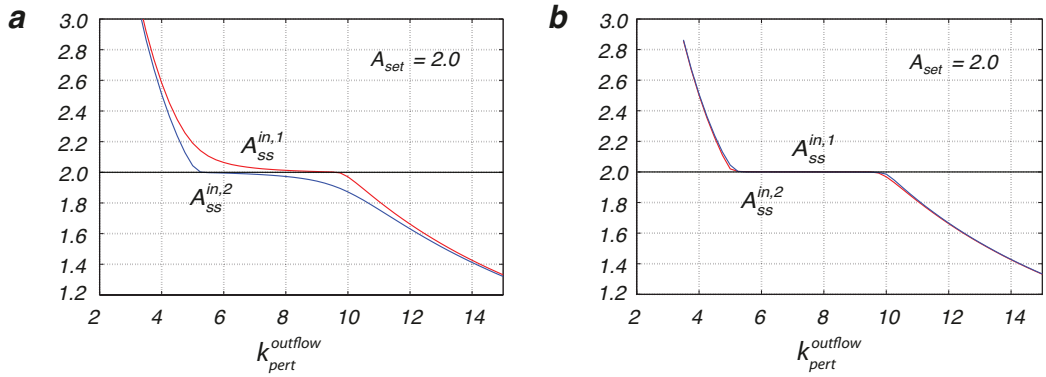

Figure S7: Comparing inflow controller 1 and 2 when both controllers have saturation kinetics in their compensatory fluxes. A cross section of the the steady state levels of A at k_{pert}^{inflow}=10 as a function of $k_{pert}^{outflow}$ is shown with set-points $A_{set}^{in,1}$=$A_{set}^{in,2}$=2.0. Because the compensatory fluxes have saturation kinetics no upper limit in E is introduced as has been done in Fig. 2a in the main paper (Fig. S6). In panel a, the controllers have $K_M^{E_{set,1}}$=$K_M^{E_{set,2}}$=1·10^{-3}. Panel b shows the same cross section, but using a higher controller accuracy, i.e. $K_M^{E_{set,1}}$=$K_M^{E_{set,2}}$=1·10^{-5}.

When controller accuracies are relative low the steady state profiles of A for controller 1 and 2 are somewhat different (Fig. S7a). A_{ss} for controller 1 is closest to its set-point at higher $k_{pert}^{outflow}$ values, while A_{ss} for controller 2 is closest to its set-point at lower $k_{pert}^{outflow}$ values. At higher controller accuracies these differences disappear and the steady state levels in A are practically identical (Fig. S7b). We conclude that the performance of E-activating and E-inhibiting controllers is mostly dependent on the kinetics of the compensatory fluxes and the parameter values of the controllers, but not on the structure of the negative feedback loop with respect to activating or inhibiting processes.

Outflow Controller Motifs

Controller Motif 5

The rate equations for motif 5 are:

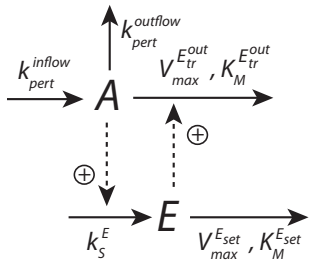

$$\dot{A} = k_{pert}^{inflow} - k_{pert}^{outflow} \cdot A - \frac{V_{max}^{E_{tr}^{out}} \cdot A}{K_M^{E_{tr}^{out}} + A} \cdot E \quad \text{(S31)}$$

$$\dot{E} = k_s^E \cdot A - \frac{V_{max}^{E_{set}} \cdot E}{K_M^{E_{set}} + E} \quad \text{(S32)}$$

The equation for $\dot{E}$ is the same as for inflow controller 2 (Eq. S18), and hence, the integral gain K_i and the measurement function A_{meas} are the same as for the inflow 2 controller, see Table 1 in main paper.

Controller Motif 6

The rate equations for motif 6 are:

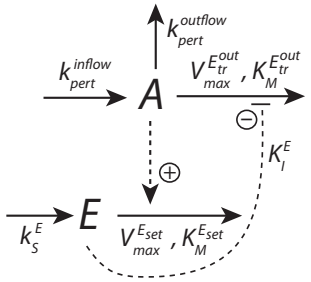

$$\dot{A} = k_{pert}^{inflow} - k_{pert}^{outflow} \cdot A - \frac{V_{max}^{E_{tr}^{out}} \cdot A}{(K_M^{E_{tr}^{out}} + A)} \cdot \frac{K_I^E}{(K_I^E + E)} \quad \text{(S33)}$$

$$\dot{E} = k_s^E - \frac{V_{max}^{E_{set}} \cdot E}{K_M^{E_{set}} + E} \cdot A \quad \text{(S34)}$$

The equation for $\dot{E}$ is the same as for inflow controller 1 (Eq. S14), and hence, the integral gain K_i and the measurement function A_{meas} are the same as for the inflow 1 controller, see Table 1 in main paper.

Controller Motif 7

The rate equations for motif 7 are:

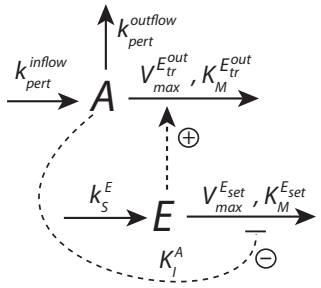

$$\dot{A} = k_{pert}^{inflow} - k_{pert}^{outflow} \cdot A - \frac{V_{max}^{E_{tr}^{out}} \cdot A}{K_M^{E_{tr}^{out}} + A} \cdot E \tag{S35}$$

$$\dot{E} = k_s^E - \frac{V_{max}^{E_{set}} \cdot E}{(K_M^{E_{set}} + E)} \cdot \frac{K_I^A}{(K_I^A + A)} \tag{S36}$$

The equation for $\dot{E}$ is the same as for inflow controller 4 (Eq. S26), and hence, the integral gain K_i and the measurement function A_{meas} are the same as for the inflow 4 controller, see Table 1 in main paper.

Controller Motif 8

The rate equations for motif 8 are:

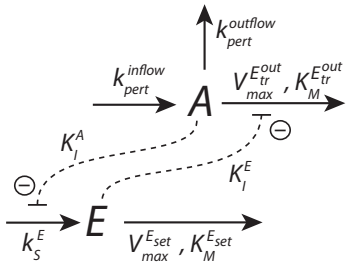

$$\dot{A} = k_{pert}^{inflow} - k_{pert}^{outflow} \cdot A - \frac{V_{max}^{E_{tr}^{out}} \cdot A}{(K_M^{E_{tr}^{out}} + A)} \cdot \frac{K_I^E}{(K_I^E + E)} \tag{S37}$$

$$\dot{E} = k_s^E \cdot \frac{K_I^A}{K_I^A + A} - \frac{V_{max}^{E_{set}} \cdot E}{K_M^{E_{set}} + E} \tag{S38}$$

The equation for $\dot{E}$ is the same as for inflow controller 3 (Eq. S22), and hence, the integral gain K_i and the measurement function A_{meas} are the same as for the inflow 3 controller, see Table 1 in main paper.

Steady state values of activating and inhibiting outflow controllers

Reference is made to Fig. 2b in main paper. The parameter values for the outflow 5 controller (adding subscript 5 to the parameters and variables in Eqs. S31 and S32 for unique identification) are $k_s^{E_5}$=0.5, $V_{max}^{E_{set,5}}$=1.0, $K_M^{E_{set,5}}$=1·10^{-3}, $V_{max}^{E_{tr}^{out,5}}$=0.5, and $K_M^{E_{tr}^{out,5}}$=1·10^{-4}.

The parameter values for the outflow 6 controller (adding subscript 6 to the parameters and variables in Eqs. S33 and S34 for unique identification) are $k_s^{E_6}$=1.0, $V_{max}^{E_{set,6}}$=0.5,

$K_M^{E_{set,6}}$=1·10^{-3}, $V_{max}^{E_{tr}^{out,6}}$=10.0, $K_M^{E_{tr}^{out,6}}$=1·10^{-4}, and $K_I^{E_6}$=1·10^{-2}.

Fig. 2 in main paper (reprintet in Fig. S8) show typical steady state values of A using activating outflow (outflow 5) and inhibiting controllers (outflow 6).

Initial concentrations: A=0.0, E_5=1.0, and E_6=1.0. The perturbations k_{pert}^{inflow} and $k_{pert}^{outflow}$ are varied between 1 and 20, and between 1 and 10, respectively, with interval of 0.5.

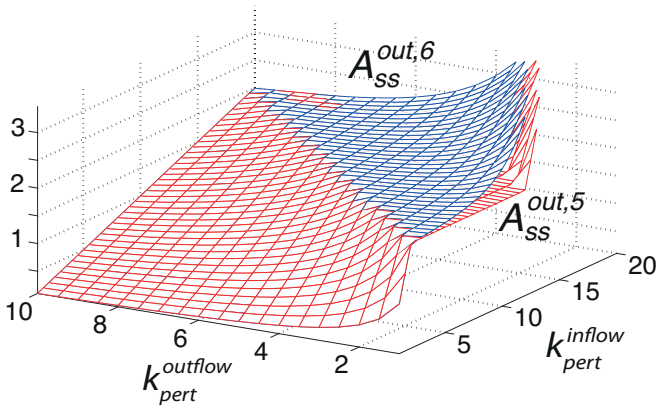

Figure S8: Fig. 2b from main paper. Steady state levels of A ($A_{ss}^{out,5}$ and $A_{ss}^{out,6}$) using outflow controller motif 5 and 6, respectively. The homeostatic set-points are $A_{set}^{out,5} = A_{set}^{out,6} = 2.0$. The better homeostatic performance of motif 5 compared to motif 6 is clearly seen. As discussed for Fig. S6, the better homeostatic performance of the E-activating controller is due to the fact that the compensatory flux for controller 5 is fixed to first-order kinetics with respect to E (Eq. S31). If the first-order compensatory flux in controller 5 is replaced by Eq. S8 the overall better homeostatic performance of controller 5 is lost similar to the situation shown for controller 1 in Fig. S7.

Loss of Homeostasis Versus Accuracy

Reference is made to the section *Set-point determination and controller accuracy* in the main paper. In Fig. S9 we illustrate the difference between loss of homeostasis (controller breakdown) and controller accuracy α, where changes in controller accuracy are represented by variations in the parameter $K_M^{E_{set}}$. Fig. S9 (panels a and b) show how inflow controller 1 can show homeostatic breakdown at inflow perturbations with high k_{pert}^{inflow} values, while controller accuracy is decreased as $K_M^{E_{set,1}}$ increases (using subscript 1 for unique identification). The theoretical set-point is $A_{set}^{in,1}$=0.5. The rate constants used are

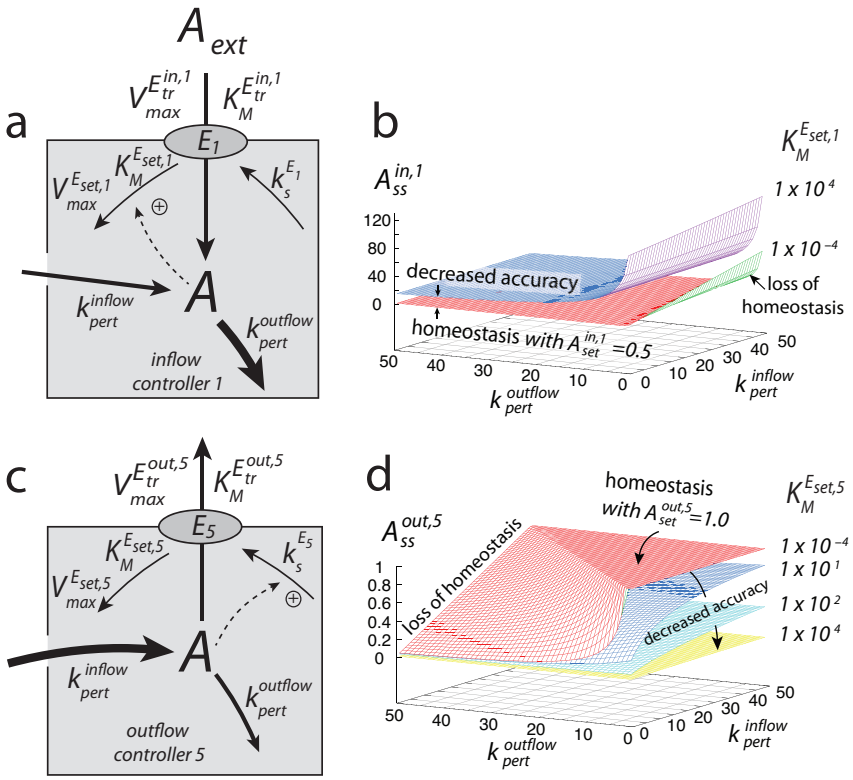

Figure S9: The $K_M^{E_{set}}$ parameter affects controller accuracy. (a) Representation of inflow controller type 1 (Eqs. S13 and S14). (b) Steady state values of A ($A_{ss}^{in,1}$) as a function of $k_{pert}^{outflow}$ and k_{pert}^{inflow} illustrating the decrease in controller accuracy with increasing $K_M^{E_{set,1}}$ values (Eq. S14). At high k_{pert}^{inflow} values relative to $k_{pert}^{outflow}$, the inflow controller looses the ability to maintain homeostasis and the compensatory flux goes to zero. This represents the lower j_A border of the homeostatic region (see Eq. 1 with description in main paper). (c) Representation of outflow controller 5 (Eqs. S31 and S32). (d) Steady state values of A ($A_{ss}^{out,5}$) as a function of $k_{pert}^{outflow}$ and k_{pert}^{inflow} illustrating the decrease in controller accuracy with increasing $K_M^{E_{set,5}}$ values. At high $k_{pert}^{outflow}$, the outflow controller looses the ability to maintain homeostasis and the compensatory flux goes to zero.

as follows: $k_s^{E_1}$=0.5, $V_{max}^{E_{set,1}}$=1.0, $V_{max}^{E_{tr}^{in,1}}$=1.0, and $K_M^{E_{tr}^{in,1}}$=1·10^{-3}.

Panels c and d show how outflow controller 5 can suffer from loss of homeostasis at outflow perturbations with high $k_{pert}^{outflow}$ values. A decreased controller accuracy is observed as $K_M^{E_{set,5}}$ increases (using subscript 5 for unique identification). The theoretical set-point is $A_{set}^{out,5}$=1.0. The rate constants are as follows: $k_s^{E_5}$=1.0, $V_{max}^{E_{set,5}}$=1.0, $V_{max}^{E_{tr}^{out,5}}$=1.0, and $K_M^{E_{tr}^{out,5}}$=1·10^{-3}.

Initial concentrations: A_{ext}=1.0, A=0.0, E_1=1.0, and E_5=1.0. The perturbations k_{pert}^{inflow} and $k_{pert}^{outflow}$ are varied between 1 and 50 with intervals of 0.5.

Graphical presentation of the accuracy

Reference is made to the section *Set-point determination and controller accuracy* and Table 1 in the main paper. Here, Fig. S10 gives a graphical presentation of controllers' accuracies α as a function of E, $K_M^{E_{set}}$ and K_I^A for $A_{set} = 2$.

From Fig. S10 we see that the accuracies take different forms and that for motifs 1/6 and 3/8 they become largest at small values of E due to $f(E) = \frac{E}{K_M^{E_{set}}+E}$. It is important to emphasize that for motifs 1/6 and 3/8 no homeostatic breakdown occurs at this high deviations from the set-point, because the E-mediated compensatory fluxes are not saturated.

At low E values, $\alpha_{2,5}$ is positive and approaches $\alpha_{2,5} = 2$, i.e. the steady state value of A_{ss} approaches zero. This can also be seen in Figs. 2a and 2c of the main paper for $A_{ss}^{in,2}$ and $E_{ss}^{in,2}$, and in Figs. 2b and 2d for $A_{ss}^{out,5}$ and $E_{ss}^{out,5}$. Similarily, at low E values, $\alpha_{1,6}$ is negative and $\alpha_{1,6} \to -\infty$, i.e. the steady state value of A_{ss} increases infinitely. This can also be seen in main paper in Figs. 2a and 2c for $A_{ss}^{in,1}$ and $E_{ss}^{in,1}$, and in Figs. 2b and 2d for $A_{ss}^{out,6}$ and $E_{ss}^{out,6}$.

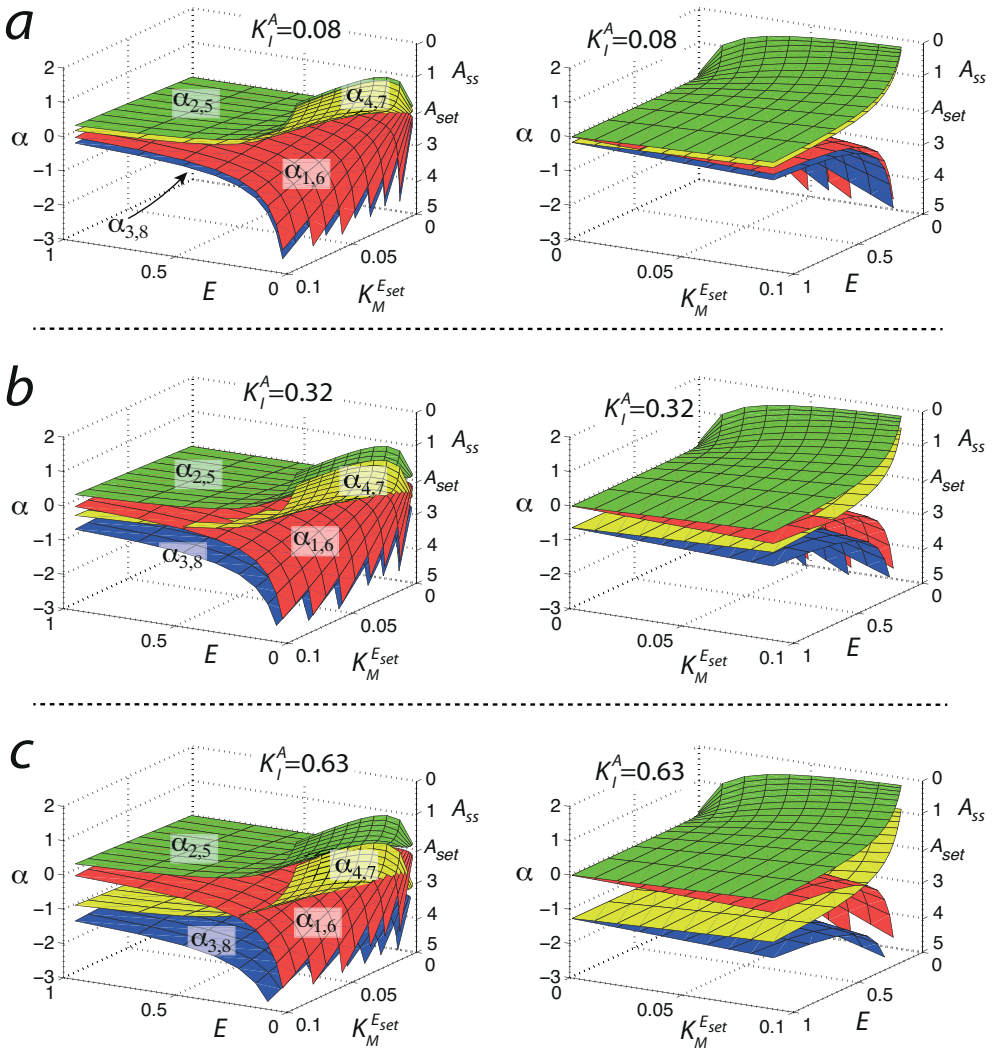

Figure S10: Steady state levels of the accuracies listed in Table 1 in main paper for $A_{set} = 2$. For unique identification we added motif numbers as subscripts, e.g. $\alpha_{2,5}$ is the accuracy for the inflow 2/outflow 5 controllers. In order to show all sides, the 3-dimensional surfaces are shown twice, where the right figures show the surfaces to the left but are rotated by 90 degrees. To increase readability, the corresponding A_{ss} values are included on a second z-axis. The value of E is varied between 0.01 and 1, $K_M^{E_{set}}$ is varied between 0.001 and 0.1. The values of K_I^A are 0.08, 0.32 and 0.63 (panels a, b and c, respectively). When $K_M^{E_{set}} \ll E$, α is small. Due to the relative high K_I^A values in panels b and c, α remains large for the motifs 3, 8 and 4, 7. Since $\alpha_{2,5}$ and $\alpha_{1,6}$ are independent of K_I^A, these surfaces do not change in panels a, b and c. The surfaces for $\alpha_{1,6}$ and $\alpha_{3,8}$ continue towards larger negative values as $E \to 0$, but are for presentation purposes limited at $\alpha = -3$.

Combination of Controllers

Reference is made to the section *Controllers' hierarchical dominance*. Here we show typical representations of steady state levels in A when using different set-point combinations of coupled inflow and outflow controllers with and without controller capacity limitations.

Fig. S11 shows the combination between inflow controller 1 and outflow controller 5 (using subscript 1 and 5 for unique identification):

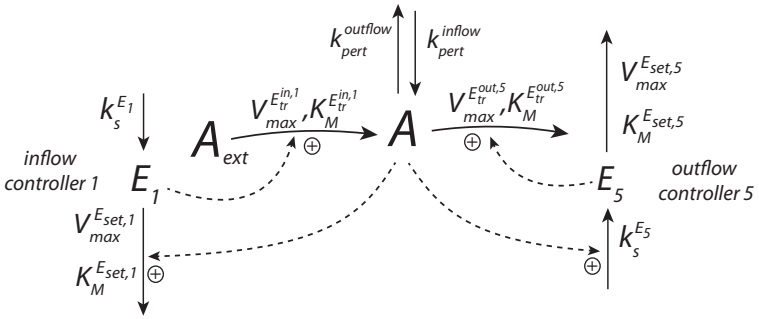

Figure S11: Motif using combined controllers 1 and 5.

The rate equations for the combined system becomes:

$$\dot{A} = k_{pert}^{inflow} - k_{pert}^{outflow} \cdot A + \frac{V_{max}^{E_{tr}^{in,1}} \cdot A_{ext}}{K_M^{E_{tr}^{in,1}} + A_{ext}} \cdot E_1 - \frac{V_{max}^{E_{tr}^{out,5}} \cdot A}{K_M^{E_{tr}^{out,5}} + A} \cdot E_5 \tag{S39}$$

$$\dot{E}_1 = k_s^{E_1} - \frac{V_{max}^{E_{set,1}} \cdot E_1}{(K_M^{E_{set,1}} + E_1)} \cdot A \tag{S40}$$

$$\dot{E}_5 = k_s^{E_5} \cdot A - \frac{V_{max}^{E_{set,5}} \cdot E_5}{(K_M^{E_{set,5}} + E_5)} \tag{S41}$$

Combination 1, $A_{set}^{in,1} < A_{set}^{out,5}$, without controller capacity limitations

In this example, the theoretical set-points are $A_{set}^{in,1}$=0.5 and $A_{set}^{out,5}$=1.0. The rate constants are as follows: $k_s^{E_1}$=0.5, $V_{max}^{E_{set,1}}$=1.0, $K_M^{E_{set,1}}$=1·10^{-3}, $V_{max}^{E_{tr}^{in,1}}$=5.0, $K_M^{E_{tr}^{in,1}}$=1·10^{-4}, $k_s^{E_5}$=1.0, $V_{max}^{E_{set,5}}$=1.0, $K_M^{E_{set,5}}$=1·10^{-3}, $V_{max}^{E_{tr}^{out,5}}$=5.0, and $K_M^{E_{tr}^{out,5}}$=1·10^{-4}. Initial concentrations: A_{ext}=1.0, A=0.0, E_1=1.0, and E_5=1.0. The perturbations k_{pert}^{inflow} and $k_{pert}^{outflow}$ are varied between 1 and 50 with intervals of 0.5.

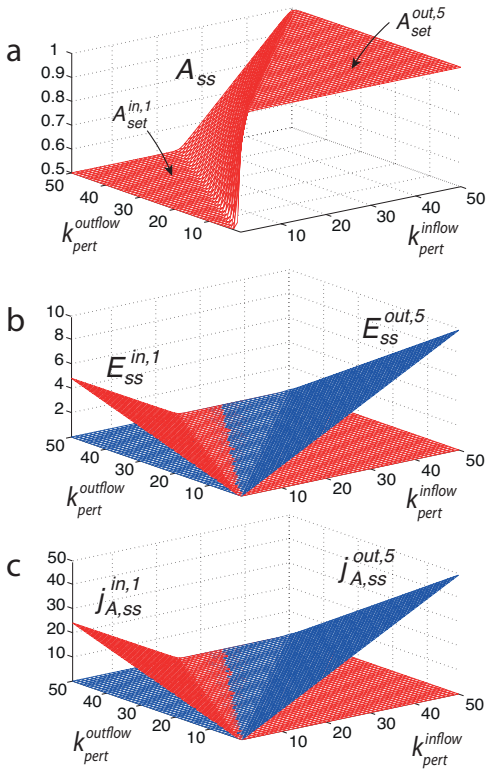

Figure S12: Controller **Combination 1**, $A_{set}^{in,1}<A_{set}^{out,5}$. Panel a: The steady state values of A (A_{ss}) as a function of k_{pert}^{inflow} and $k_{pert}^{outflow}$. Panel b: The steady state values of $E_{ss}^{in,1}$ and $E_{ss}^{out,5}$ as a function of k_{pert}^{inflow} and $k_{pert}^{outflow}$. Panel c: The steady state fluxes of A, $j_{A,ss}^{in,1}$ and $j_{A,ss}^{out,5}$, as a function of k_{pert}^{inflow} and $k_{pert}^{outflow}$. The set points are $A_{set}^{in,1}$=0.5 and $A_{set}^{out,5}$=1.0.

The results in Fig. S12a show steady state values of A (A_{ss}) similar to Fig. 4h in the main paper. In addition, we show the steady state values of the controllers $E_{ss}^{in,1}$ and $E_{ss}^{out,5}$ (Fig. S12b), together with the corresponding steady state compensatory fluxes of A, $j_{A,ss}^{in,1}$ and $j_{A,ss}^{out,5}$ (Fig. S12c). The three panels (Fig. S12a-c) represent the same situations as shown in Fig. 4 by panels b, d and f.

Combination 1, $A_{set}^{in,1}<A_{set}^{out,5}$, with controller capacity limitations

To illustrate the effect of capacity limitation on the region of homeostasis in combined controllers, we use again the motif in Fig. S11, where the capacity limit of inflow controller 1 is $j_{A,max}^{in,1} = 2$ and $j_{A,max}^{out,5} = 3$ for outflow controller 5.

The theoretical set-points are $A_{set}^{in,1}$=0.5 and $A_{set}^{out,5}$=1.0, and the rate constants are as follows: $k_s^{E_1}$=0.5, $V_{max}^{E_{set,1}}$=1.0, $K_M^{E_{set,1}}$=1·10^{-3}, $V_{max}^{E_{tr}^{in,1}}$=1.0, $K_M^{E_{tr}^{in,1}}$=1·10^{-4}, $k_s^{E_5}$=1.0, $V_{max}^{E_{set,5}}$=1.0, $K_M^{E_{set,5}}$=1·10^{-3}, $V_{max}^{E_{tr}^{out,5}}$=1.0, and $K_M^{E_{tr}^{out,5}}$=1·10^{-4}. Initial concentrations: A_{ext}=1.0, A=0.0, E_1=1.0, and E_5=1.0. The perturbations k_{pert}^{inflow} are varied between 1 and 7 and $k_{pert}^{outflow}$ are varied between 1 and 11, both with intervals of 0.2.

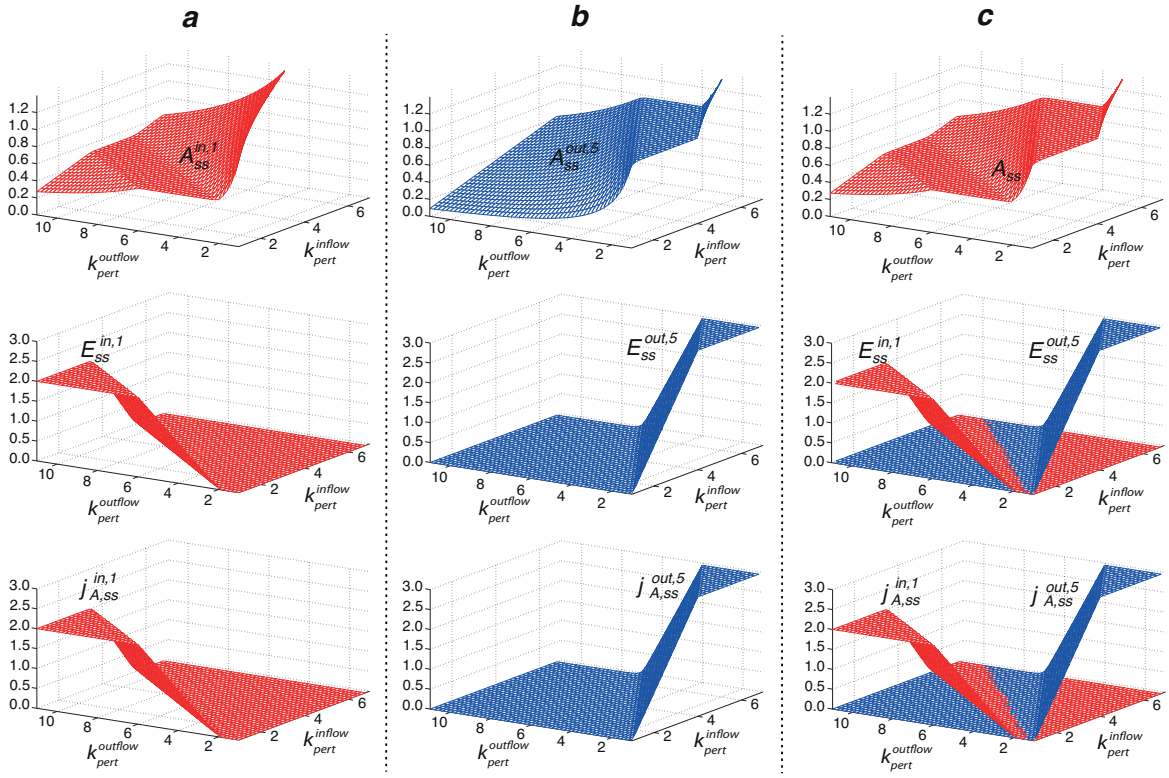

Figure S13: Illustration of homeostatic region for combined controllers with capacity limitations. Panel a: Steady state levels of $A_{ss}^{in,1}$, $E_{ss}^{in,1}$ and $j_{A,ss}^{in,1}$ for inflow controller 1 alone. Panel b: Steady state levels of $A_{ss}^{out,5}$, $E_{ss}^{out,5}$ and $j_{A,ss}^{out,5}$ for outflow controller 5 alone. Panel c: Steady state levels of A_{ss}, $E_{ss}^{in,1}/E_{ss}^{out,5}$ and $j_{A,ss}^{in,1}/j_{A,ss}^{out,5}$ in the combined controller.

From Fig. S12 and Fig. S13c we see that the borders of the overall homeostatic region for the combined controller are due to the lower and upper borders in the compensatory flux j_A. The lower border ($j_A = 0$) is due to the homeostatic breakdown in ideal controllers as indicated in Fig. 1b in the main paper. The upper border is due to the applied capacity

limits for j_A.

Combination 3, $A_{set}^{in,1}>A_{set}^{out,5}$, without controller capacity limitations

In this example, the theoretical set-points are $A_{set}^{in,1}$=2.0 and $A_{set}^{out,5}$=1.0. The rate constants are as follows: $k_s^{E_1}$=1.0, $V_{max}^{E_{set,1}}$=0.5, $K_M^{E_{set,1}}$=1·10^{-3}, $K_M^{E_{tr}^{in,1}}$=1·10^{-4}, $k_s^{E_5}$=1.0, $V_{max}^{E_{set,5}}$=1.0, $K_M^{E_{set,5}}$=1·10^{-3}, and $K_M^{E_{tr}^{out,5}}$=1·10^{-4}. The perturbations k_{pert}^{inflow} and $k_{pert}^{outflow}$ are varied between 1 and 50 with interval of 0.5.

Dependent on the value of $V_{max}^{E_{tr}^{in,1}}$ relative to the value of $V_{max}^{E_{tr}^{out,5}}$, either the inflow or the outflow controller dominates the homeostatic behavior of the system, see Fig. S14.

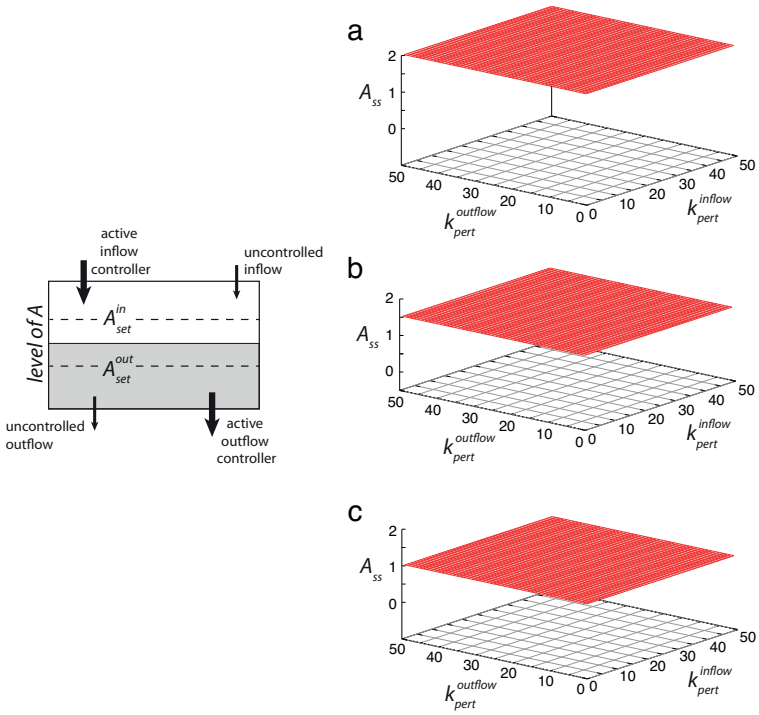

Figure S14: A_{ss} levels and homeostatic behaviors of combined controllers 1 and 5 with $A_{set}^{in,1}$=2.0 and $A_{set}^{out,5}$=1.0, such that $A_{set}^{in}>A_{set}^{out}$ and both controllers being active. Dependent on $V_{max}^{E_{tr}^{in,1}}$ relative to $V_{max}^{E_{tr}^{out,5}}$, either the inflow controller (panel a, high $V_{max}^{E_{tr}^{in,1}}$ compared to $V_{max}^{E_{tr}^{out,5}}$) or the outflow controller (panel c, low $V_{max}^{E_{tr}^{in,1}}$ compared to $V_{max}^{E_{tr}^{out,5}}$) determines the homeostatic behavior of the system. If $V_{max}^{E_{tr}^{in,1}}$ and $V_{max}^{E_{tr}^{out,5}}$ are of the same size, A_{ss} settles between A_{set}^{in} and A_{set}^{out} (panel b).

At high $V_{max}^{E_{tr}^{in,1}}$ values relative to $V_{max}^{E_{tr}^{out,5}}$ i.e. $V_{max}^{E_{tr}^{in,1}}$=1.0 and $V_{max}^{E_{tr}^{out,5}}$=0.2, the outflow controller is less effective compared to the inflow controller, and inflow controller 1 determines the system's steady state levels in A, which now are close to the theoretical set-point $A_{set}^{in,1}$=2.0, see Fig. S14a.

If $V_{max}^{E_{tr}^{in,1}}$=$V_{max}^{E_{tr}^{out,5}}$ = 1.0, the controllers are equally strong, and the steady state of A ends up in between the set points as shown in Fig. S14b.

At low $V_{max}^{E_{tr}^{in,1}}$ values relative to $V_{max}^{E_{tr}^{out,5}}$, i.e. $V_{max}^{E_{tr}^{in,1}}$=0.2 and $V_{max}^{E_{tr}^{out,5}}$=1.0, the inflow controller is less effective compared to the outflow controller. The outflow controller 5 determines the system's steady state values in A, which are close to the theoretical set-point $A_{set}^{out,5}$=1.0, see Fig. S14c.

Activated Pathways

Reference is made to Fig. 5a in the main paper where controller motifs 1 and 5 are combined. The rate equations are as follows:

$$\dot{A} = k_{pert}^{inflow} \cdot A_{ext} + \frac{V_{max}^{E_{tr}^{in,1}} \cdot A_{ext}}{K_M^{E_{tr}^{in,1}} + A_{ext}} \cdot E_1 - k_{path}^{ess} \cdot A - \frac{V_{max}^{E_{tr}^{out,5}} \cdot A}{K_M^{E_{tr}^{out,5}} + A} \cdot E_5 \tag{S42}$$

$$\dot{E_1} = k_s^{E_1} - \frac{V_{max}^{E_{set,1}} \cdot E_1}{K_M^{E_{set,1}} + E_1} \cdot A \tag{S43}$$

$$\dot{E_5} = k_s^{E_5} \cdot A - \frac{V_{max}^{E_{set,5}} \cdot E_5}{K_M^{E_{set,5}} + E_5} \tag{S44}$$

The external concentration of A, (A_{ext}), is kept constant but at different levels. The flux of the essential and 'overflow' pathways are given as

$$j_1 = k_{path}^{ess} \cdot A \tag{S45}$$

$$j_2 = \frac{V_{max}^{E_{tr}^{out,5}} \cdot A}{K_M^{E_{tr}^{out,5}} + A} \cdot E_5 \tag{S46}$$

respectively. The specific growth rate μ is related to the external concentration of A by Monod's equation (2, 3):

$$\mu = \mu_{max} \cdot \frac{A_{ext}}{K_s + A_{ext}} \tag{S47}$$

Parameter values used in the calculation of Fig. 5c are: k_{pert}^{inflow}=0.2, k_{path}^{ess}=0.5, $k_s^{E_1}$=0.05, $V_{max}^{E_{set,1}}$=0.05, $K_M^{E_{set,1}}$=0.1, $V_{max}^{E_{tr}^{in,1}}$=0.1, $K_M^{E_{tr}^{in,1}}$=$1{\cdot}10^{-3}$, $k_s^{E_5}$=0.05, $V_{max}^{E_{set,5}}$=0.1, $K_M^{E_{set,5}}$=0.5, $V_{max}^{E_{tr}^{out,5}}$=0.1, $K_M^{E_{tr}^{out,5}}$=$1{\cdot}10^{-3}$, μ_{max}=0.85, and K_s=10.0. Initial concentrations: A=0.5, E_1=0.05, E_5=$1{\cdot}10^{-3}$.

Integral Windup in Combined Controllers

Integral windup is the occurrence of an unlimited growth of the manipulated variable E (integrated error). In the main paper we saw that integral windup can occur due to capacity problems of the controller, i.e., limitations in the compensatory flux j_A or in E.

In order to determine whether an integral windup situation will occur with a specific combination of controllers, we refer to Fig. S15a, where the signs of the derivatives of the manipulated variables are given for each controller motif. We then organize the controllers according to their set points along the axis of steady state A-values, as shown in Fig. S15b for the example of combined inflow 1 and outflow 5 controllers with $A_{set}^{in,1} > A_{set}^{out,5}$. This corresponds to **Combination 3** in main paper and the situation described in Fig. S14b.

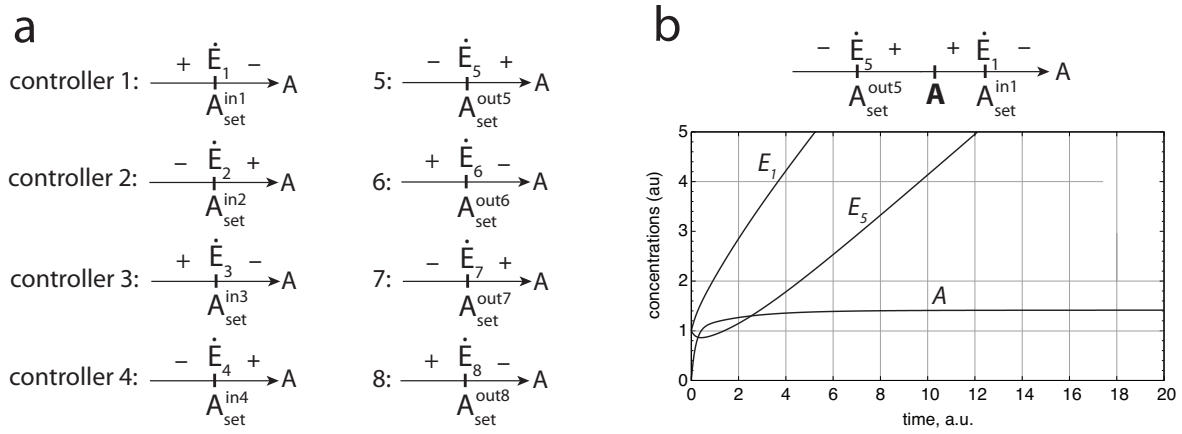

Figure S15: Determination of possible windup behavior using combined controllers. (a) Sign-change of $\dot{E}_i$ for the eight controllers $i \in \{1, ..., 8\}$ as a function of steady state concentration in A. At $A = A_{set}$ we have $\dot{E}_i = 0$. Positive and negative signs along the A-axis show where $\dot{E}_i$ is positive or negative for controller i. (b) Inflow 1 and outflow 5 controller combination with $A_{set}^{in,1} = 2.0$, $A_{set}^{out,5} = 1.0$, $k_{pert}^{inflow} = k_{pert}^{outflow} = 5.0$. Both controllers are active and the steady state value in A lies between $A_{set}^{in,1}$ and $A_{set}^{out,5}$. $V_{max}^{E_{tr}^{in,1}}$ = $V_{max}^{E_{tr}^{out,5}}$ =1.0 as shown for Fig. S14b. Because $\dot{E}_1 > 0$ and $\dot{E}_5 > 0$ at this A_{ss}-value, integral windup is observed for both E_1 and E_5.

As seen from Fig. S15b, integral windup will occur since the steady state value of A will end up between the set points where both manipulated variables have positive derivatives and therefore growing E-levels.

Integral Windup for Combined Inflow Controllers 1 and 2

In order to illustrate how integral windup can occur using two inflow controllers (the situation described as **Combination 4**, $A_{set}^{in,i} > A_{set}^{in,j}$, in main paper), we use the combination of inflow 1 and inflow 2 controllers shown in Fig. S16:

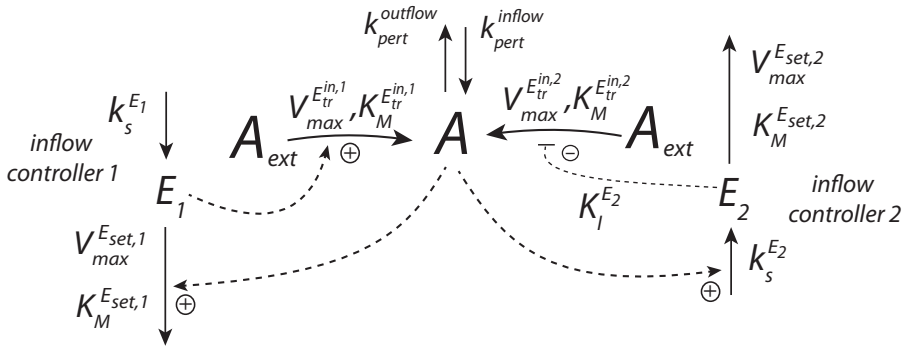

Figure S16: Motif using combined controllers 1 and 2.

The rate equations of combined inflow controllers 1 and 2 are given by Eqs. S48-S50.

$$\dot{A} = k_{pert}^{inflow} - k_{pert}^{outflow} \cdot A + \frac{V_{max}^{E_{tr}^{in,1}} \cdot A_{ext}}{(K_M^{E_{tr}^{in,1}} + A_{ext})} \cdot E_1 + \frac{V_{max}^{E_{tr}^{in,2}} \cdot A_{ext}}{(K_M^{E_{tr}^{in,2}} + A_{ext})} \cdot \frac{K_I^{E_2}}{(K_I^{E_2} + E_2)} \tag{S48}$$

$$\dot{E}_1 = k_s^{E_1} - \frac{V_{max}^{E_{set,1}} \cdot E_1}{K_M^{E_{set,1}} + E_1} \cdot A \tag{S49}$$

$$\dot{E}_2 = k_s^{E_2} \cdot A - \frac{V_{max}^{E_{set,2}} \cdot E_2}{K_M^{E_{set,2}} + E_2} \tag{S50}$$

For the simulation shown in Fig. S17a, the applied rate constants are: $k_s^{E_1}$=2.0, $V_{max}^{E_{set,1}}$=1.0, $K_M^{E_{set,1}}$=1·10^{-3}, $V_{max}^{E_{tr}^{in,1}}$=4.0, $K_M^{E_{tr}^{in,1}}$=1·10^{-3}, $k_s^{E_2}$=1.0, $V_{max}^{E_{set,2}}$=3.0, $K_M^{E_{set,2}}$=1·10^{-3}, $V_{max}^{E_{tr}^{in,2}}$=40, $K_M^{E_{tr}^{in,2}}$=1·10^{-3}, and $K_I^{E_2}$=1.0. Hence, the homeostatic set-point for controller 1 is $A_{set}^{in,1}$=2.0 and for controller 2 $A_{set}^{in,2}$=3.0. For the simulation shown in Fig. S17b, the applied rate constants are similar, except $V_{max}^{E_{set,2}}$=1.0. Hence, in this simulation the homeostatic set-point for controller 1 is $A_{set}^{in,1}$=2.0 and for controller 2 $A_{set}^{in,2}$=1.0.

For both simulations, the level of perturbation is k_{pert}^{inflow}=1.0 and $k_{pert}^{outflow}$=10.0 and the initial concentrations are A=0.0, E_1=1.0, and E_2=1.0.

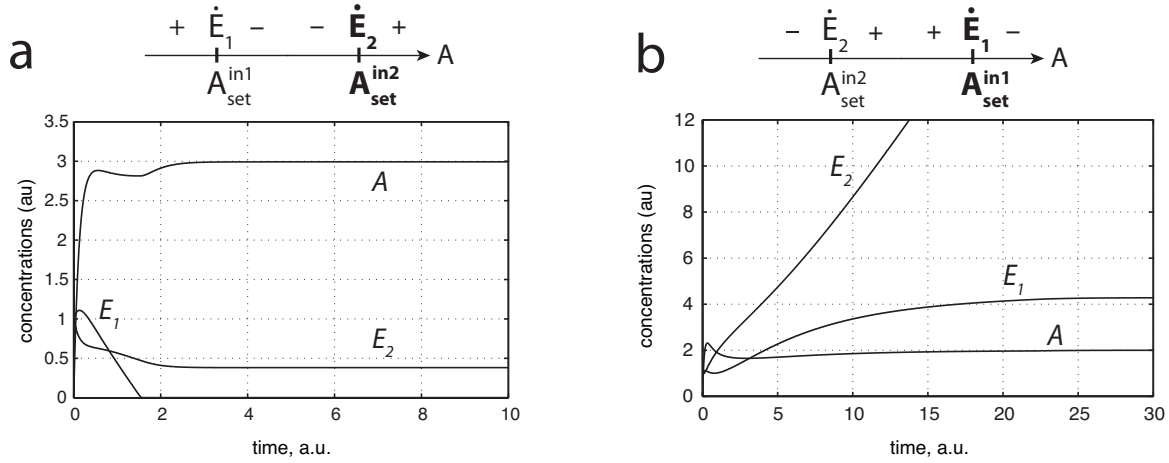

Figure S17: Example of **Combination 4**, $A_{set}^{in,i} > A_{set}^{in,j}$, (see main paper) using inflow controllers 1 and 2. (a) A high outflow perturbation rate ($k_{pert}^{outflow}$=10) from A and a relative low inflow perturbation rate (k_{pert}^{inflow}=1) to A with set-points $A_{set}^{in,2}$=3.0 > $A_{set}^{in,1}$=2.0. Due to the higher set-point of inflow controller 2 the steady state value of A is $A_{set}^{in,2} = 3.0$ as long as the outflow rate from A is larger than the inflow rate to A. At $A_{ss} = A_{set}^{in,2} = 3.0$, $\dot{E}_2 = 0$ and $\dot{E}_1 < 0$ as indicated by the schematic representation above the graph and the numerical result. (b) Same system as in (a), but set-point for inflow controller 2 has been changed from 3.0 to 1.0 by using $V_{max}^{E_{set,2}}$=1.0. Now inflow controller 1 dominates and we have $A_{ss} = A_{set}^{in,1} = 2.0$. However, at this value of A_{ss}, $\dot{E}_2 > 0$, and integral windup in E_2 is observed.

Integral Windup for Combined Inflow 2 and Outflow 6 Controllers

The occurrence of integral windup is for some controller combinations dependent of the inflow/outflow perturbations acting on the system. To illustrate this phenomenon we use the combination of inflow 2 and outflow 6 controllers as shown in Fig. S18.

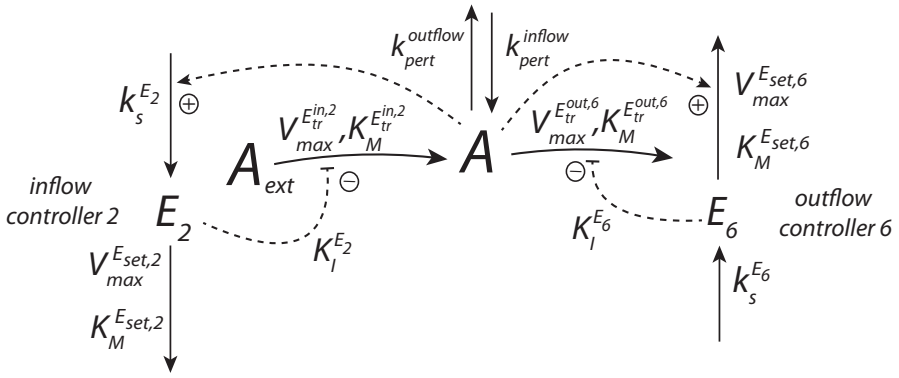

Figure S18: Motif using combined controllers 2 and 6.

The rate equations of combined inflow controllers 2 and 6 are given by Eqs. S51-S52.

$$\dot{A} = k_{pert}^{inflow} - k_{pert}^{outflow} \cdot A + \frac{V_{max}^{E_{tr}^{in,2}} \cdot A_{ext}}{(K_M^{E_{tr}^{in,2}} + A_{ext})} \cdot \frac{K_I^{E_2}}{(K_I^{E_2} + E_2)} - \frac{V_{max}^{E_{tr}^{out,6}} \cdot A}{(K_M^{E_{tr}^{out,6}} + A)} \cdot \frac{K_I^{E_6}}{(K_I^{E_6} + E_6)} \tag{S51}$$

$$\dot{E}_2 = k_s^{E_2} \cdot A - \frac{V_{max}^{E_{set,2}} \cdot E_2}{K_M^{E_{set,2}} + E_2} \tag{S52}$$

$$\dot{E}_6 = k_s^{E_6} - \frac{V_{max}^{E_{set,6}} \cdot E_6}{K_M^{E_{set,6}} + E_6} \cdot A \tag{S53}$$

For the simulations shown in Fig. S19 (panels a,b and c) the applied rate constants are: $k_s^{E_2}$=1.0, $V_{max}^{E_{set,2}}$=1.0, $K_M^{E_{set,2}}$=1·10^{-5}, $V_{max}^{E_{tr}^{in,2}}$=2.0, $K_M^{E_{tr}^{in,2}}$=1·10^{-3}, $K_I^{E_2}$=0.1, $k_s^{E_6}$=2.0, $V_{max}^{E_{set,6}}$=1.0, $K_M^{E_{set,6}}$=1·10^{-5}, $V_{max}^{E_{tr}^{out,6}}$=2.0, $K_M^{E_{tr}^{out,6}}$=1·10^{-3}, and $K_I^{E_6}$=0.1. Hence, the homeostatic set-point for controller 2 is $A_{set}^{in,2}$=1.0 and for controller 6 $A_{set}^{out,6}$=2.0, which corresponds to **Combination 1**, $A_{set}^{in} < A_{set}^{out}$ (see main paper).

For the simulation shown in Fig. S19d reference is made to **Combination 3**, $A_{set}^{in} > A_{set}^{out}$, in main paper. The homeostatic set-point for controller 2 is $A_{set}^{in,2}$=2.0 and for controller 6 $A_{set}^{out,6}$=1.0. The applied rate constants are the same as for Fig. S19, panels a,b and c, but with the following exceptions: $V_{max}^{E_{set,2}}$=2.0 and $k_s^{E_6}$=1.0.

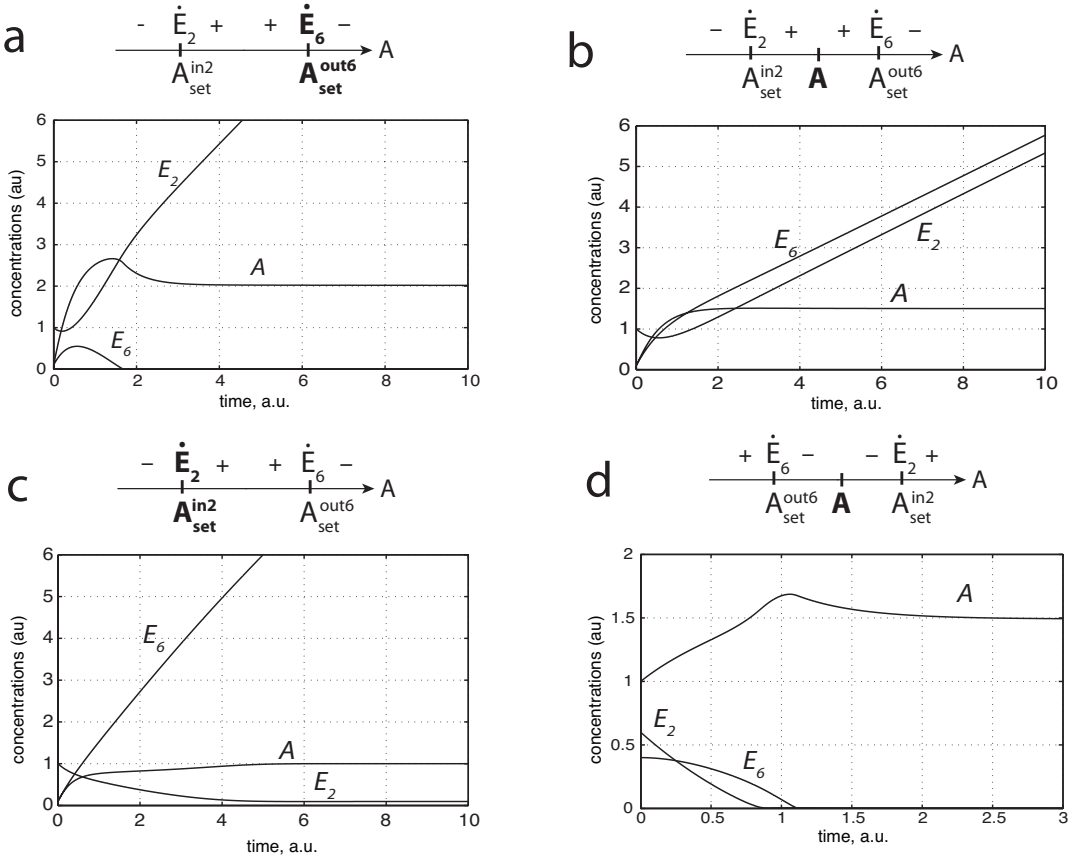

Figure S19: Different windup and non-windup situations for the combination of inflow 2 and outflow 6 controllers organized as **Combination 1** (panels a, b, and c) and **Combination 3** (panel d). (a) Dominanting inflow perturbation, i.e. k_{pert}^{inflow}=6.0 and $k_{pert}^{outflow}$=2.0, drives the steady state level of A towards $A_{set}^{out,6}$=2.0. The level of E_6 is low, which corresponds to least possible inhibition and maximum E-mediated compensatory outflux j_A, see Eq. S2. Integral windup is observed in E_2 as the sign of $\dot{E}_2$ is positive at $A_{ss} = A_{set}^{out,6}$. (b) Balancing inflow and outflow perturbations, i.e. k_{pert}^{inflow}=3.0 and $k_{pert}^{outflow}$=2.0, leading to no compensatory influx or outflux j_A (corresponds to Fig. 4d in main paper). Integral windup is observed for both controllers E_2 and E_6. (c) Dominanting outflow perturbation, i.e. k_{pert}^{inflow}=3.0 and $k_{pert}^{outflow}$=4.0, drives the steady state level of A towards $A_{set}^{in,2}$=1.0. The level of E_2 is low, which corresponds to least possible inhibition and maximum E-mediated compensatory influx j_A, see Eq. S1. Integral windup is observed in E_6 as the sign of $\dot{E}_6$ is positive at $A_{ss} = A_{set}^{in,2}$. (d) Reorganized set points, i.e. $A_{set}^{in,2} > A_{set}^{out,6}$, using balancing inflow and outflow perturbations (k_{pert}^{inflow}=3.0 and $k_{pert}^{outflow}$=2.0), leading to maximum compensatory influx and outflux j_A (corresponds to Fig. S14b). No integral windup is observed for the manipulated variables E_2 and E_6.

Controller Motifs in Physiology

Below we give brief descriptions of the homeostatic controller motifs that have been identified in the literature.

Iron Homeostasis

Mammalian Iron Homeostasis In mammalian iron homeostasis both inflow and outflow controllers can be identified. At low iron concentrations, iron-homeostasis can be described by inflow controller type 1, where IRP2 together with IRP1 (playing the role of E) stabilize mRNAs of iron-utilizing proteins by binding to iron-responsive elements (4) and activate the flow of iron into the cell by transferrin receptors (5, 6). In turn, as iron levels increase, IRP2 is subject to an iron-dependent proteasomal degradation mediated by the F-box protein FBXL5, which becomes stabilized as iron concentrations increase (7, 8), see Fig. S20.

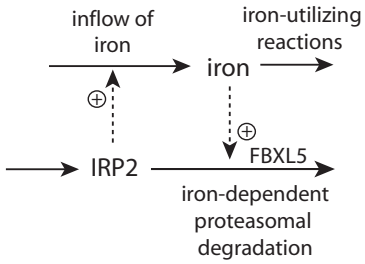

Figure S20: At low iron levels or high demands for iron an inflow controller motif 1 can be identified as part of mammalian iron homeostasis.

At high iron concentrations active IRP levels are low due to the proteasomal IRP2 degradation and the functional change of IRP1 to an aconitase (4) allowing an outflow controller scheme 5 to take over by exporting iron out of the cell using the iron-induced transporter ferroportin, relating to E in scheme 5, see also Fig. S21.

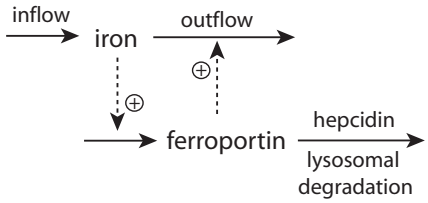

Figure S21: At high iron levels the outflow controller motif 5 can be identified as part of mammalian iron homeostasis.

Hepcidin (9) regulates ferroportin by binding to it, which leads to ferroportin's internalization and degradation. Hepcidin has a relative strong binding to ferroportin (9), that indicates a possible zero-order degradation of ferroportin defining the iron set-point at high iron concentrations.

Plant Iron Homeostasis. As plants grow mostly in soil at neutral pH and under aerobic conditions when iron is highly insoluble, plants have only limited access to iron and have therefore developed strategies to facilitate the uptake of iron (10–12). On the other hand iron concentrations inside plant cells are maintained within a relatively small range to avoid iron toxicity. In Arabidopsis, IRON-REGULATED-TRANSPORTER1 (IRT1) is the major high affinity transporter for iron uptake. IRT1 is subject to an iron-induced turnover (13) leading to a negative feedback regulation in iron uptake of controller motif 1, as indicated in Fig. S22. Due to a plant's high demand for iron at neutral soil pH and aerobic conditions, it is not surprising that plants have developed a homeostatic mechanism based on an inflow controller type. So far, no outflow control scheme for iron regulation has been described for plants.

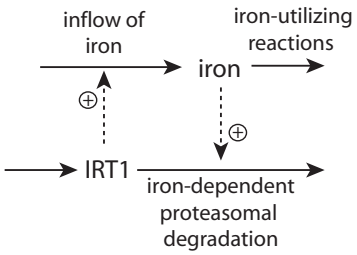

Figure S22: At low iron levels and therefore high demands for iron an inflow controller motif 1 can be identified as part of iron homeostasis in plants.

Iron and Zinc Homeostasis in Yeast. In yeast, uptake of iron occurs, besides using high affinity siderophores, by Fet3p-Ftr1p, a protein-complex which is induced by the iron sensing transcription factors Aft1p and Aft2p (14, 15). Transport of iron through Ftr1p leads to an iron-dependent internalization of Fet3p-Ftr1p and its degradation by the ubiquitin-proteasome pathway (16), showing an inflow regulatory structure as in controller 1, where Fet3p-Ftr1p plays the role of E.

Interestingly, in yeast, the zinc transporter ZRT1 is also subject to a zinc-dependent ubiquitination and endocytosis similar to that described for the iron-specific Fet3p-Ftr1p system (17) suggesting an inflow-based homeostatic mechanism 1 for zinc.

An additional control mechanism for iron homeostasis based on outflow controller type 6 has been identified in yeast, where Aft1p activates Cth2, which specifically downregulates mRNAs encoding proteins that participate in many Fe-dependent and consuming processes

(18). With increasing iron concentrations the Aft1p-mediated formation of Cth2 is decreased as Aft1p is actively shuttled out of the nucleus (19), relating E by the combined roles of Aft1p and Cth2, see Fig. S23.

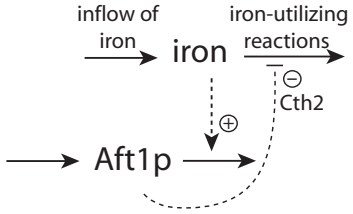

Figure S23: Control motif 6 in yeast iron homeostasis. Transcription factor Aft1p leads to a Cth2-mediated inhibition of iron-utilizing reactions. Aft1p is exported out of the nucleus in an iron-dependent manner.

Iron Homeostasis in Bacteria and Acidophiles In *E. coli* and other bacteria iron homeostasis is mediated by the iron sensor Fur, a protein which is activated at high cellular iron levels and represses the transcription of most iron-acquisition genes by binding to their promoters (20). In addition, Fur also represses RyhB, a small RNA (sRNA), which functions as a post-transcriptional repressor of iron-utilizing genes (20) analogous to the role of E in outflow controller 8. Thus, high iron levels lead to the repression of RyhB, which on its side inhibits iron-using genes. An outflow control structure has probably developed, as *E. coli* under anaerobic conditions needs to cope with soluble iron, which at high concentrations is toxic. The usage of sRNAs as inhibitors has the advantage of being efficient in terms of cellular energy usage as they do not require new protein synthesis. Fur-based outflow control structures appear also to occur in acidophiles living at the highest levels of soluble iron(21), but the molecular mechanisms for iron homeostasis in acidophiles are so far unknown. Living at high soluble iron concentrations outflow control structures for iron homeostasis are anticipated to be employed in acidophiles, see Fig. S24.

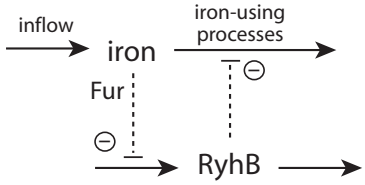

Figure S24: Control motif 8 in bacterial iron homeostasis. High iron levels lead to a Fur-mediated shut-down in the expression of RyhB (20).

Heme Homeostasis

Heme, an iron-containing porphyrin, is an important cofactor for many proteins including the transport and storage of oxygen by hemoglobin and myoglobin, respectively, and the transport of electrons by cytochromes. Because heme can cause oxidative stress when it reacts with molecular oxygen its concentration is under homeostatic control. Recently, heme concentrations were found to be negatively regulated by Rev-erbα (22) (a member of the nuclear receptor superfamily of ligand-regulated transcription factors), by inhibiting PGC-1α, a key metabolic transcriptional regulator. These results indicate that the negative feedback loop may be inflow controllers of types 2 or 4. In *Drosophila*, the homolog of Rev-erbα, E75, binds heme, regulating E75 function by increasing its stability (23). Thus, it appears that inflow controller 4 is a possible candidate for the homeostatic regulation of heme in flies and mammals, see Fig. S25. Interestingly, besides regulating heme homeostasis Rev-erbα is also implicated in the coordination of the mammalian circadian clock acting there as a negative regulator of BMAL1 (24, 25), as well as in glucose homeostasis and energy metabolism (26), clearly showing the complex relationships between homeostatic and adaptive (circadian) mechanisms.

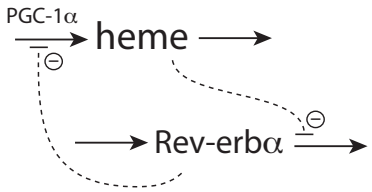

Figure S25: Regulation of heme homeostasis by inflow controller type 4 is supported by the observations that Rev-erbα reduces heme levels by repressing heme synthesis through PGC-1α inhibition (22), and the heme-mediated stabilization of Rev-erbα (23).

Copper Homeostasis

Copper is an essential element needed in electron transfer reactions, but becomes toxic at higher concentrations. In *Saccharomyces cerevisiae* the transporter Ctr1p plays a critical role in the uptake of copper. Ctr1p is a high affinity transporter having a $K_M^{E_{set}}$ of 1 to 5 μM copper (22). Ooi *et al.* (27) showed that Ctr1p is degraded by a specific copper-dependent pathway indicating a homeostatic mechanism to that of inflow control motif 1. Liu *et al.* (28) showed that the copper-dependent (proteasomal) degradation of Ctr1p is mediated by the Rsp5 ubiquitin ligase.

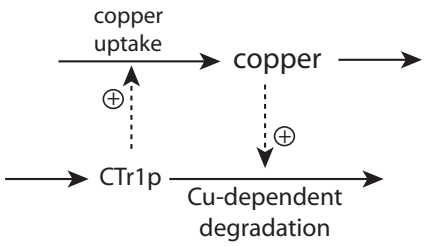

Figure S26: Copper regulation has been observed by a controller type 1 mechanism, where the transporter for the uptake of copper, Ctr1p, is degraded in a copper-dependent manner (27).

Interestingly, Wu *et al.* (29) found recently that there is an additional regulatory mechanism related to the C-terminal end of Ctr1p, which upon excess of copper leads to a rapid inhibition of copper transport by Ctr1p. This may be related to the presence of additional parallel inflow control mechanisms described by controller motifs 2 and/or 4.

Blood Calcium Homeostasis

Blood calcium levels are subject to negative feedback regulation where calcitonin (CT), parathyroid hormone (PTH) and the active form of vitamin D, calcitriol, are important factors involved in the regulation of calcium and bone metabolism.

Hypocalcemia

When calcium levels are low PTH stimulates calcium uptake by the release of calcium from the bone and by stimulating the production of the active form of vitamin D, calcitriol (1,25-dihydroxycholecalciferol). Calcitriol induces synthesis of calcium binding protein in intestinal epithelial cells leading to absorption of calcium into the blood. Habener *et al.* (30) studied the dynamics of bovine PTH to alterations in the concentrations of extracellular calcium. The authors found that secretion of some PTH continued despite high concentrations of calcium (5mM), and biosynthesis of ProPTH changed only slightly. The conversion of ProPTH to PTH was found to be independent of the extracellular calcium concentration. At high calcium concentrations a large fraction (up to 50%) of newly synthesized PTH was found to be rapidly and completely degraded within the tissue. These data suggest that the parathyroid cell contains a calcium-sensitive degradative pathway for PTH and that a inflow controller type 1 for Ca homeostasis takes place, see Fig. S27.

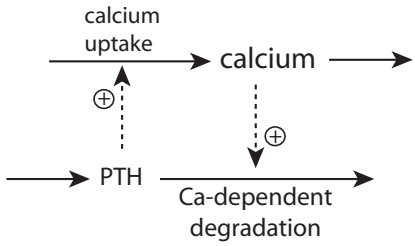

Figure S27: Work by Habener *et al.* (30) found that secretion of PTH is independent to changes in extracellular calcium, and that at high calcium levels a large fraction of PTH is degraded, leading to a type 1 inflow control mechanism.

It has also been well established that increases in extracellular calcium concentration inhibit PTH secretion (31, 32), as in inflow controller motif 3, see Fig. S28.

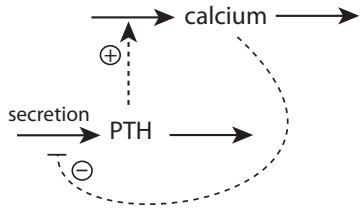

Figure S28: Inhibition of PTH secretion by extracellular calcium indicates a type 3 inflow control mechanism.

There is an interesting connection between PTH degradation and the inhibition of PTH secretion. Fujita *et al.* (33) found that a PTHase splits PTH into several fragment peptides. The amino-terminal peptide was found to participate in the autoregulation of PTH secretion, inhibiting PTH secretion both *in vivo* in humans and *in vitro* in dispersed bovine parathyroid cells. There may be different PTH degradation mechanisms possibly due to different type 3 inflow control mechanisms.

El-Samad *et al.* (34) suggested a related mechanism based on integral control, where the concentration in PTH is considered to be proportional to the error between the actual calcium concentration and its set-point, and where the rate of calcitriol production is proportional to the PTH concentration. Thus, the integrated value of PTH, relating to the calcitriol concentration (which leads to the absorption of calcium) will lead to calcium levels adapting perfectly to the calcium set-point. However, the authors do not describe the physicochemical processes how the error in the calcium concentration is sensed and related to the amount of PTH.

In the here given representations of inflow controller types 1 or 3 the error in calcium

concentration is not related to the PTH concentration, but to the overall change (rate) in PTH. This implies that the PTH concentration at the calcium set-point is constant and in a steady state, while the model by El-Samad *et al.* suggest that the PTH concentration at the calcium set-point should be zero. Contrary to that suggestion, experimental results showed (35) that the plasma PTH steady state concentration in a healthy young man at normocalcemia conditions lies around 3 pmol/L with a PTH secretion rate fluctuating between 0.5 and 1.0 pmol/(L min).

Hypercalcemia

Calcitonin (CT) is a peptide hormone whose secretion from the thyroid glands is regulated by increased concentrations of extracellular calcium maintaining calcium homeostasis. The calcium-dependent activation of CT is due to a serial double inhibition, where calcium derepresses the transcriptional repressor DREAM (downstream regulatory element antagonist modulator) (36). CT functions as an inhibitor of bone resorption, decreases serum calcium levels and defends against hypercalcemia. This regulation of calcium homeostasis at high calcium (outflow) conditions has been found to be mediated by the calcium-sensing receptor (CaSR), independent of the CaSR's involvement in the regulation of PTH (37) and conforms with a type 5 controller, see Fig. S29.

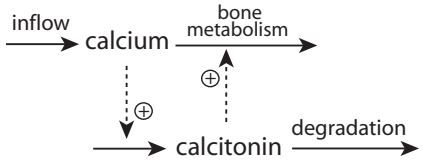

Figure S29: The described feedback of the homeostatic regulation at high calcium extracellular levels occurs by an outflow type 5 controller. Calcium activates the expression of calcitonin by derepressing the transcriptional inhibitor DREAM. Calcitonin functions as an inhibitor of bone resorption and lowers the levels of calcium by bone metabolism and other processes.

Regulation of calcitonin degradation appears to be one of the factors to influence calcium homeostasis. Baylin *et al.* (38) found that in patients with hypercalcemia, calcitonin is much more rapidly degraded compared to healthy persons maintaining calcium homeostasis.

Oxygen Homeostasis

Metazoan cells depend upon the utilization of O_2 for their metabolic processes and keep, dependent on the cell type, the cellular O_2 concentration within a narrow range at differ-

ent set-points (39). In all metazoan cells regulation of this oxygen homeostasis occurs via hypoxia-inducible factor 1 (HIF-1). HIF-1 was discovered in 1992 as a protein required for hypoxia-induced transcription of the human *EPO* gene encoding erythropoietin, which is the hormone that controls red blood cell production and thereby determines the transport of oxygen in the blood (40). HIF-1 is a heterodimeric protein consisting of a constitutively expressed HIF-1β subunit and an O_2-regulated HIF-1α subunit. HIF-1α is degraded by the 26S proteasome in an O_2-dependent manner mediated by prolyl hydroxylase domain proteins (PHDs) (41). Thus, the regulation of O_2 by HIF-1α occurs by a type 1 homeostatic inflow controller, see Fig. S30.

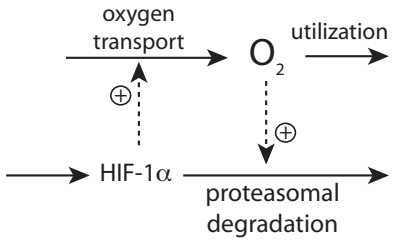

Figure S30: In oxygen homeostasis a negative feedback type 1 inflow controller can be identified where HIF-1α activates the transport of oxygen, but HIF-1α is subject to proteasomal degradation in an O_2-dependent manner.

HIF-1α interacts with many other cellular proteins, indicating how interwoven oxygen homeostasis is with cellular and systemic physiology (41).

Stem Cell Homeostasis in Plant Meristems

During growth, plants maintain in their apical meristems a certain number of undifferentiated cells (stem cells), from which roots and shoot are produced. The stem cell homeostasis in *Arabidopsis* shoots has been described (42, 43) by the interaction between two key factors, the transcription factor WUSCHEL (WUS), which is required for the maintenance of stem cells and the peptide CLAVATA3 (CLV3), which is secreted from the stem cells and inhibits WUS expression. This negative feedback between WUS and CLV3 is a type 2 inflow controller (Fig. S31), which may lead to homeostatic controlled WUS levels to ensure proper growth.

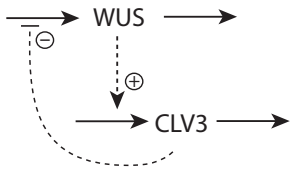

Figure S31: A type 2 inflow controller appears operative in the stem cell homeostasis in *Arabidopsis* shoots (42).

Thyroid Hormone Homeostasis

The iodine-containing thyroid hormones tetraiodothyronine (T_4) and triiodothyronine (T_3) have important functions including the regulation/increase of oxygen and energy consumption rates, body temperature regulation, and the turnover of minerals in bone. The major controlling factor of T_3 and T_4 production and release is the thyroid-stimulating hormone TSH, which is activated by the thyrotropin-releasing hormone (TRH). The thyroid gland produces large amounts of T_4, but T_3 is primarily responsible for the observed effects of thyroid hormones. Among other tasks, deiodinase D2 can convert T_4 into T_3, while deiodinase D3 is involved in the degradation of T_3 (44). The thyroid hormone is under homeostatic control and a negative feedback in T_3 has been identified. In the absence of T_3, the thyroid hormone (nuclear) receptor TR binds to a repression complex containing co-repressor molecules and histone deacetylases leading to the expression of TRH. The presence of T_3 prevents the repression complex from interacting with the TR, allowing the complex to remain at the promoter and leading to repression (45). Thus, T_3 inhibits its own synthesis by inhibiting the expression of TRH/TSH and generating a type 3 inflow controller, see Fig. S32.

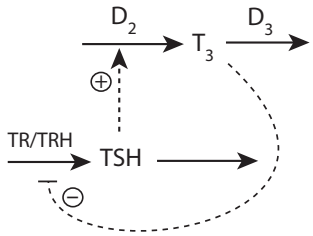

Figure S32: A type 3 inflow controller is operative in the T_3 thyroid hormone homeostasis.

Brassinosteroid Homeostasis

Brassinosteroids (BRs) are steroid hormones which are important for plant growth and development. For example, in BR-deficient mutants dwarfism is observed, while BR in

excess leads to abnormal organ growth (46). The BRs are recognized by cell-surface receptor BRI1, which then by two successive inhibition (degradation) reactions result in unphosphorylated and active BZR1 and BZR2 (BES1). Binding of BZR1 to the consensus sequence CGTG(T/C)G at promoter regions of different genes in the BR synthesis pathway leads to the repression of BR production (47). BZR1 is phosphorylated by the GSK3-like kinase BIN2, indicating degradation by the proteasome (48) and leading to a type 2 inflow controller, see Fig. S33.

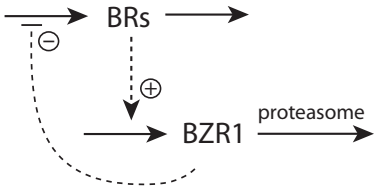

Figure S33: At the transcriptional level a type 2 inflow controller can be identified in BR homeostasis. The activation of BZR1 involves two serial inhibitory (degradation) processes while repression of BR biosynthesis genes occur by the binding of BZR1 to their promoter regions.

Interestingly, homeostasis of active BRs is also regulated by a metabolic outflow controller that inactivate/degrade BRs. It has been found that Brassinolide (BL, the most active BR) activates the enzyme BAS1. BAS1 participates in the catabolism of BRs by transforming BL into an inactive form (46) defining a type 5 outflow controller, see Fig. S34.

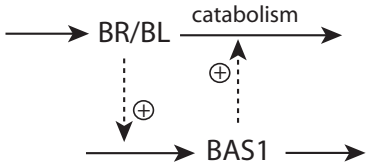

Figure S34: At the metabolic level a type 5 outflow controller can be identified in BR homeostasis. BL, the most active form of BRs, stimulates the expression of the BR-degrading enzyme BAS1, which is involved in the catabolism of BRs.

Blood Glucose Homeostasis

Blood glucose homeostasis is achieved by the hormones insulin and glucagon. At high blood glucose levels β-cells in the pancreas secrete insulin. Insulin triggers a series of phosphorylation reactions to activate glycogen synthase, which catalyzes the conversion of into glycogen in the liver defining a type 5 outflow controller, see Fig. S35.

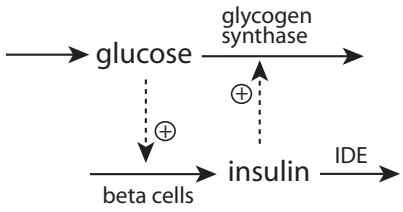

Figure S35: Outflow controller type 5 in the insulin-mediated blood glucose homeostasis.

As shown in the description of motif 5, robust homeostasis may be achieved when the degradation in E, i.e. here insulin, is of zero-order. Insulin has a short half-life (4-6 min) and is degraded by a specific insulin-degrading enzyme (IDE) (49). Reported insulin-$K_M^{E_{set}}$ values of mammalian IDE from the database BRENDA (www.brenda-enzymes.org) range between approximately 10-200 nM, while insulin concentrations have been reported to vary between 0.1-2 nM (50). Because the reported $K_M^{E_{set}}$ values for insulin are generally higher than the reported insulin concentration, it appears that outflow controller 5 (Fig. S35) may not be able to enforce robust glucose homeostasis alone, but possibly in interaction with the glucagon-mediated inflow controller (see next paragraph).

Glucogon is a hormone that is secreted by α-cells in the pancreas. Glucagon initiates a series of phosphorylation reactions leading to the activation of glycogen phosphorylase, which catalyzes the breakdown of glycogen into glucose leading to an increase in glucose concentration. At high glucose concentrations the production of glucagon is inhibited, but is increased when glucose concentration is decreased, suggesting that a type 3 inflow controller is operative at low glucose concentrations. Degradation of glucagon occurs by a glucagon-degrading enzyme (GDE) (51, 52) (Fig. S36).

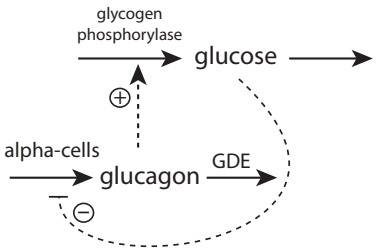

Figure S36: Inflow controller type 3 in the glucagon-mediated blood glucose homeostasis.

Interestingly, released glucagon stimulates the increase of insulin via produced cAMP (53) such that both controllers appear to be operative near the set-point, which possibly increases the robustness of the combined homeostatic controllers.

Supporting References

1. Radhakrishnan, K., and A. C. Hindmarsh, 1993. Description and Use of LSODE, the Livermore Solver for Ordinary Differential Equations. NASA Reference Publication 1327, Lawrence Livermore National Laboratory Report UCRL-ID-113855. National Aeronautics and Space Administration, Lewis Research Center, Cleveland, OH 44135-3191.

2. Monod, J., 1949. The Growth of Bacterial Cultures. *Annu Rev Microbiol* 3:371–94.

3. Gaudy, A. F., A. Obayashi, and E. T. Gaudy, 1971. Control of Growth Rate by Initial Substrate Concentration at Values below Maximum Rate. *Appl Microbiol* 22:1041–47.

4. Rouault, T. A., 2006. The role of iron regulatory proteins in mammalian iron homeostasis and disease. *Nat Chem Biol* 2:406–414.

5. Andrews, N. C., and P. J. Schmidt, 2007. Iron homeostasis. *Annu Rev Physiol* 69:69–85.

6. Rouault, T. A., 2009. Cell biology. An ancient gauge for iron. *Science* 326:676–7.

7. Salahudeen, A. A., J. W. Thompson, J. C. Ruiz, H. W. Ma, L. N. Kinch, Q. Li, N. V. Grishin, and R. K. Bruick, 2009. An E3 ligase possessing an iron-responsive hemerythrin domain is a regulator of iron homeostasis. *Science* 326:722–6.

8. Vashisht, A. A., K. B. Zumbrennen, X. Huang, D. N. Powers, A. Durazo, D. Sun, N. Bhaskaran, A. Persson, M. Uhlen, O. Sangfelt, C. Spruck, E. A. Leibold, and J. A. Wohlschlegel, 2009. Control of iron homeostasis by an iron-regulated ubiquitin ligase. *Science* 326:718–721.

9. Nemeth, E., M. S. Tuttle, J. Powelson, M. B. Vaughn, A. Donovan, D. M. Ward, T. Ganz, and J. Kaplan, 2004. Hepcidin regulates cellular iron efflux by binding to ferroportin and inducing its internalization. *Science* 306:2090–3.

10. Briat, J.-F., C. Curie, and F. Gaymard, 2007. Iron utilization and metabolism in plants. *Current Opinion in Plant Biology* 10:276–282.

11. Walker, E. L., and E. L. Connolly, 2008. Time to pump iron: iron-deficiency-signaling mechanisms of higher plants. *Current Opinion in Plant Biology* 11:530–535.

12. Jeong, J., and M. L. Guerinot, 2009. Homing in on iron homeostasis. *Trends in Plant Science* 14:280–285.

13. Kerkeb, L., I. Mukherjee, I. Chatterjee, B. Lahner, S. D. E., and E. L. Conolly, 2008. Iron-induced Turnover of the Arabidopsis IRON-REGULATED TRANSPORTER1 Metal Transporter Requires Lysine Residues. *Plant Physiol* 146:1964–1973.

14. Kaplan, C. D., and J. Kaplan, 2009. Iron acquisition and transcriptional regulation. *Chem Rev* 109:4536–52.

15. Yamaguchi-Iwai, Y., R. Stearman, A. Dancis, and R. D. Klausner, 1996. Iron-regulated DNA binding by the AFT1 protein controls the iron regulon in yeast. *EMBO J* 15:3377–84.

16. Felice, M. R., I. De Domenico, L. Li, D. McVey Ward, B. B., G. Musci, and K. J., 2005. Post-transcriptional regulation of the yeast high affinity iron transport system. *J Biol Chem* 280:22181–22190.

17. Gitan, R. S., and D. J. Eide, 2000. Zinc-regulated ubiquitin conjugation signals endocytosis of the yeast ZRT1 zinc transporter. *Biochem J* 346:329–336.

18. Puig, S., E. Askeland, and D. J. Thiele, 2005. Coordinated remodeling of cellular metabolism during iron deficiency through targeted mRNA degradation. *Cell* 120:99–110.

19. Ueta, R., N. Fujiwara, K. Iwai, and Y. Yamaguchi-Iwai, 2007. Mechanism underlying the iron-dependent nuclear export of the iron-responsive transcription factor Aft1p in Saccharomyces cerevisiae. *Mol Biol Cell* 18:2980–90.

20. Massé, E., and M. Arguin, 2005. Ironing out the problem: new mechanisms of iron homeostasis. *Trends Biochem Sci* 30:462–468.

21. Osorio, H., V. Martinez, P. A. Nieto, D. S. Holmes, and R. Quatrini, 2008. Microbial iron management mechanisms in extremely acidic environments: comparative genomics evidence for diversity and versatility. *BMC Microbiol* 8:203.

22. Wu, N., L. Yin, E. A. Hanniman, S. Joshi, and M. A. Lazar, 2009. Negative feedback maintenance of heme homeostasis by its receptor, Rev-erbalpha. *Genes Dev* 23:2201–9.

23. Reinking, J., M. M. Lam, K. Pardee, H. M. Sampson, S. Liu, P. Yang, S. Williams, W. White, G. Lajoie, A. Edwards, and H. M. Krause, 2005. The Drosophila nuclear receptor E75 contains heme and is gas responsive. *Cell* 122:195–207.

24. Emery, P., and S. M. Reppert, 2004. A rhythmic Ror. *Neuron* 43:443–6.

25. Yin, L., and M. A. Lazar, 2005. The orphan nuclear receptor Rev-erbalpha recruits the N-CoR/histone deacetylase 3 corepressor to regulate the circadian Bmal1 gene. *Mol Endocrinol* 19:1452–9.

26. Yin, L., N. Wu, J. C. Curtin, M. Qatanani, N. R. Szwergold, R. A. Reid, G. M. Waitt, D. J. Parks, K. H. Pearce, G. B. Wisely, and M. A. Lazar, 2007. Rev-erbalpha, a heme sensor that coordinates metabolic and circadian pathways. *Science* 318:1786–9.

27. Ooi, C. E., E. Rabinovich, A. Dancis, J. S. Bonifacino, and R. D. Klausner, 1996. Copper-dependent degradation of the Saccharomyces cerevisiae plasma membrane copper transporter Ctr1p in the apparent absence of endocytosis. *EMBO J* 15:3515–23.

28. Liu, J., A. Sitaram, and C. G. Burd, 2007. Regulation of copper-dependent endocytosis and vacuolar degradation of the yeast copper transporter, Ctr1p, by the Rsp5 ubiquitin ligase. *Traffic* 8:1375–84.

29. Wu, X., D. Sinani, H. Kim, and J. Lee, 2009. Copper transport activity of yeast Ctr1 is down-regulated via its C terminus in response to excess copper. *J Biol Chem* 284:4112–22.

30. Habener, J. F., B. Kemper, and J. Potts, J. T., 1975. Calcium-dependent intracellular degradation of parathyroid hormone: a possible mechanism for the regulation of hormone stores. *Endocrinology* 97:431–41.

31. LeBoff, M. S., D. Shoback, E. M. Brown, J. Thatcher, R. Leombruno, D. Beaudoin, M. Henry, R. Wilson, J. Pallotta, S. Marynick, and et al., 1985. Regulation of parathyroid hormone release and cytosolic calcium by extracellular calcium in dispersed and cultured bovine and pathological human parathyroid cells. *J Clin Invest* 75:49–57.

32. Russell, J., W. Zhao, G. Christ, S. Ashok, and R. H. Angeletti, 1999. Ca2+-induced increases in steady-state concentrations of intracellular calcium are not required for inhibition of parathyroid hormone secretion. *Mol Cell Biol Res Commun* 1:221–6.

33. Fujita, T., M. Fukase, H. Baba, T. Yamaguchi, S. Takata, T. Fujimi, M. Nishikawa, and C. Nakamoto, 1992. New actions of parathyroid hormone through its degradation. *J Endocrinol Invest* 15:121–7.

34. El-Samad, H., J. P. Goff, and M. Khammash, 2002. Calcium homeostasis and parturient hypocalcemia: an integral feedback perspective. *J Theor Biol* 214:17–29.

35. Schmitt, C. P., F. Schaefer, A. Bruch, J. D. Veldhuis, H. Schmidt-Gayk, G. Stein, E. Ritz, and O. Mehls, 1996. Control of pulsatile and tonic parathyroid hormone secretion by ionized calcium. *J Clin Endocrinol Metab* 81:4236–43.

36. Matsuda, M., T. A. Yamamoto, and M. Hirata, 2006. Ca2+-dependent regulation of calcitonin gene expression by the transcriptional repressor DREAM. *Endocrinology* 147:4608–17.

37. Kantham, L., S. J. Quinn, O. I. Egbuna, K. Baxi, R. Butters, J. L. Pang, M. R. Pollak, D. Goltzman, and E. M. Brown, 2009. The calcium-sensing receptor (CaSR) defends against hypercalcemia independently of its regulation of parathyroid hormone secretion. *Am J Physiol Endocrinol Metab* 297:E915–23.

38. Baylin, S. B., A. L. Bailey, T. H. Hsu, and G. V. Foster, 1977. Degradation of human calcitonin in human plasmas. *Metabolism* 26:1345–54.

39. Semenza, G. L., 2009. Regulation of oxygen homeostasis by hypoxia-inducible factor 1. *Physiology (Bethesda)* 24:97–106.

40. Semenza, G. L., and G. L. Wang, 1992. A nuclear factor induced by hypoxia via de novo protein synthesis binds to the human erythropoietin gene enhancer at a site required for transcriptional activation. *Mol Cell Biol* 12:5447–54.

41. Semenza, G. L., 2009. Oxygen homeostasis. *Wiley Interdiscip Rev Syst Biol Med* 2:336–61.

42. Brand, U., J. C. Fletcher, M. Hobe, E. M. Meyerowitz, and R. Simon, 2000. Dependence of stem cell fate in Arabidopsis on a feedback loop regulated by CLV3 activity. *Science* 289:617–9.

43. Hohm, T., E. Zitzler, and R. Simon, 2010. A dynamic model for stem cell homeostasis and patterning in Arabidopsis meristems. *PLoS One* 5:e9189.

44. Gereben, B., A. M. Zavacki, S. Ribich, B. W. Kim, S. A. Huang, W. S. Simonides, A. Zeold, and A. C. Bianco, 2008. Cellular and molecular basis of deiodinase-regulated thyroid hormone signaling. *Endocr Rev* 29:898–938.

45. Braverman, L. E., and U. R. DL., 2005. Werner & Ingbar's the thyroid: a fundamental and clinical text. Lippincott Williams & Wilkins, Philadelphia.

46. Tanaka, K., T. Asami, S. Yoshida, Y. Nakamura, T. Matsuo, and S. Okamoto, 2005. Brassinosteroid homeostasis in Arabidopsis is ensured by feedback expressions of multiple genes involved in its metabolism. *Plant Physiol* 138:1117–25.

47. He, J. X., J. M. Gendron, Y. Sun, S. S. Gampala, N. Gendron, C. Q. Sun, and Z. Y. Wang, 2005. BZR1 is a transcriptional repressor with dual roles in brassinosteroid homeostasis and growth responses. *Science* 307:1634–8.

48. He, J. X., J. M. Gendron, Y. Yang, J. Li, and Z. Y. Wang, 2002. The GSK3-like kinase BIN2 phosphorylates and destabilizes BZR1, a positive regulator of the brassinosteroid signaling pathway in Arabidopsis. *Proc Natl Acad Sci U S A* 99:10185–90.

49. Duckworth, W. C., R. G. Bennett, and F. G. Hamel, 1998. Insulin degradation: progress and potential. *Endocr Rev* 19:608–24.

50. Gower, B. A., W. M. Granger, F. Franklin, R. M. Shewchuk, and M. I. Goran, 2002. Contribution of insulin secretion and clearance to glucose-induced insulin concentration in african-american and caucasian children. *J Clin Endocrinol Metab* 87:2218–24.

51. Kakiuchi, S., and H. H. Tomizawa, 1964. Properties of a Glucagon-Degrading Enzyme of Beef Liver. *J Biol Chem* 239:2160–4.

52. Yamaguchi, N., K. Koyama, Y. Yamamura, A. Okui, E. Konishi, T. Katayama, N. Katsuragi, T. Kurihara, H. Nakazato, and J. Imanishi, 1995. A novel proteinase, glucagon-degrading enzyme, secreted by a human pancreatic cancer cell line, HPC-YO. *J Biochem* 117:7–10.

53. Gromada, J., W. G. Ding, S. Barg, E. Renstrom, and P. Rorsman, 1997. Multisite regulation of insulin secretion by cAMP-increasing agonists: evidence that glucagon-like peptide 1 and glucagon act via distinct receptors. *Pflugers Arch* 434:515–24.